Delft University of Technology

Biomedical Engineering

Master Thesis

Application of OCT and IVUS to investigate the combined effect of plaque structural stress and wall shear stress on plaque progression in human coronary arteries

---

By

Prodromos Gavriilidis

4739469

Thesis committee:	Dr. ir. J. J. Wentzel,	Erasmus MC
	Dr. A. Akyildiz,	Erasmus MC
	Prof. dr. P. J. French	TU Delft
	Prof. dr. G. Vdovin	TU Delft

Abstract

Introduction: Atherosclerosis, the major source of cardiovascular diseases, is one of the leading causes of death. During atherosclerosis the arterial wall is affected by a complex process of lipid driven inflammation that leads to thickening of the arterial wall resulting in a so called plaque. Because of plaque growth, the lumen of the artery gradually narrows. As the lumen area is decreasing, reduction and even restriction of blood flow can occur, which can lead to a heart attack or stroke depending on the affected artery. Biomechanical stresses are known to influence the development of the disease. Those stress are the plaque structural stress (PSS) and wall shear stress (WSS) induced by the blood flow at the vessel wall. The aim of this project was to study the contribution of these biomechanical stresses and their combination to plaque progression in human coronary arteries. In order to investigate this effect a new methodology for the calculation of the stresses was introduced that utilizes the image modalities optical coherence tomography (OCT) and intravascular ultrasound (IVUS). The combination of those two image modalities can provide more accurate information regarding the plaque composition than the approaches that have been applied so far. In particular the cap thickness, which is the region shielding the lipid rich necrotic core from the blood flow, is crucial for structural stress calculations.

Methods: The new methodology consisted of three steps. During the first step image data from the image modalities optical coherence tomography (OCT) and intravascular ultrasound (IVUS) were fused. The resulted images were cross-sections of the human coronary arteries that consisted of the lumen and the outer wall obtained from IVUS and the fibrous cap obtained from OCT. However, they did not contain information about the size of the necrotic core; thus, the second step was to reconstruct the necrotic core. For that purpose an algorithm from the literature was implemented that can reconstruct the necrotic core. The produced geometry resulting from the second step consisted of the same features as those from step one but they also included the contours of the necrotic core. The third step was the calculation of the PSS using those 2D geometries. The WSS data were obtained from another study. For the statistical analysis the data of both stress calculations were ranked as low, medium and high. Two different approaches for the definition of the thresholds of those ranks were used, vessel specific and absolute thresholds. In the vessel specific approach the thresholds of the aforementioned ranks were specific for each vessel, while in the second approach the threshold values were based on the whole sample size. Those two approaches were studied in order to explore if the response of the vessels depends to the absolute values of biomechanical stresses or it is relative to their respective biomechanical stresses. Change in wall thickness was used as metric to quantify the plaque progression. In order to study the contribution of the biomechanical stresses to the plaque progression in the human coronary arteries, statistical analysis was carried out using ANOVA with plaque progression as dependent variable and PSS and WSS as independent variables.

Results: Plaque development was significantly related to WSS using both approaches to rank the WSS values into low, mid and high. In general, regions exposed to low WSS showed the most plaque progression. The individual effect of PSS was not statistically significant using both approaches, however there was a trend demonstrating that high PSS could promote plaque development. When PSS and WSS were combined using the vessel specific approach to rank the data, there was plaque progression for the cases of low WSS combined with any level of plaque structural stress. However, only WSS had a statistically significant effect in this case revealing that the resulted effect was entirely estimated by WSS. If absolute thresholds

were used for both WSS and PSS, there was no statistical effect. Despite that, there was a trend showing that high PSS combined with high WSS could promote plaque development.

Conclusions: During this project a new methodology was utilized in order to study the contribution of WSS, PSS and their combination to the plaque development in human coronary arteries. It was also the first study that utilized the combination of the image modalities OCT and IVUS in that topic. It was demonstrated that WSS could promote plaque development. PSS also enhanced plaque progression but with no statistically significant effect. Regarding the combination, it was demonstrated that the effect was explained completely by wall shear stress for the vessel specific approach. For the absolute thresholds approach, there was no statistically significant effect. However, more data are required to validate these results.

Acknowledgements

First of all, I want to express my gratitude to my daily supervisors from Erasmus MC dr.ir. Jolanda Wentzel and dr. Ali Akyildiz for the continuous guidance during all the stages of my master thesis project. Moreover, I want also to thank them along with my supervisor from TU Delft prof. dr. P.J. French for the insightful comments during the writing part of my thesis. Furthermore, I want to thank also the PhD student Eline Hartman for her help with the statistical analysis and Suze-Anne Korteland from Erasmus MC for the help during the development of the new methodology. Moreover, I want to thank all my colleagues for being friendly and creating a “gezellig” environment. Lastly, I want to express my gratitude to all my friends and family for supporting me during my studies for my master degree in biomedical engineering.

Contents

Chapter 1: Introduction

Atherosclerosis is a progressive disease of the arteries and is the most common cause promoting cardiovascular diseases (CVDs). Based on the World Health Organization CVDs are the leading causes of death universally [1]. During atherosclerosis plaque is building up inside the arterial vessel wall, increasing its local wall thickness. Upon gradual plaque growth, the lumen of the artery becomes narrowed. Since plaque growth results in lumen narrowing in the later stages of the disease only, atherosclerosis is hard to diagnose at the early stages. Therefore, the disease is asymptomatic. In its later stages, atherosclerosis can cause severe health issues associated with CVDs, such as heart attack and stroke, which can result to death.

The building-up process of the plaque and, thus, the thickening of the intimal layer of the arterial vessel wall, is a cascade of events that takes place inside the vessel wall. LDL from blood penetrates the endothelium and is introduced to the intimal layer where it is oxidized [2], see Figure 1A. Upon LDL oxidation, the endothelial cells are activated and an inflammatory response is initiated. During that, monocytes are being introduced to the vessel wall through the endothelium, where they differentiate into macrophages in order to remove the oxidized LDL from the vessel wall. When they engulf the oxidized LDL, they transform into foam cells [3], see Figure 1B. The foam cells secrete chemical factors, such as matrix metalloproteinases (MMPs), which trigger vascular smooth muscle cells from the media that are close to the inflammatory region to migrate to intima [4], see Figure 1C. The macrophages that transform to foam cells undergo apoptosis resulting in the formation of a lipid rich region. The presence of debris and the ineffective process of removing it causes vascular smooth muscle cells' death. This region that consists of the apoptotic cells and the debris is called necrotic core, see Figure 1D. The region between the endothelium and the necrotic core is called fibrous cap and it is consisted of migrated vascular smooth muscle cells. The fibrous cap functions as a shield between the blood circulation and the necrotic core. It must be mentioned that necrotic core is a component of the plaque, see Figure 2. Inflammatory cells present in the plaque produce enzymes that can break down the fibrous cap. This process makes the plaque prone to rupture. If rupture occurs, the content of the necrotic core is exposed to the blood flow and thrombus is formed. Thrombus can restrict the blood circulation from that vessel and can cause an infarction [5].

However, what can cause the plaque to rupture? There is no simple answer so far to this question. The first thing that we need to consider is the vulnerability of the plaque. The vulnerability of the plaque is connected to the plaque composition. There are the stable plaques, plaques that have a thick cap and low lipid content, and there are the vulnerable plaques, which are characterized by thin cap, lipid rich necrotic core, increased plaque inflammation, positive vascular remodelling, increased vasa-vasorum neovascularization and intra-plaque haemorrhage [6], see Figure 2. Furthermore, the presence of calcification inside the necrotic core can affect plaque stability. Calcification triggered by the apoptosis of macrophages and vascular smooth muscle cells is called microcalcification [7]. Microcalcification is associated with plaque progression [8]. The calcification of the plaque that is triggered by macrophages enhancing osteoblastic differentiation and maturation of vascular smooth muscle cells is called macrocalcification [8]. Opposing to the effect of microcalcification, macrocalcification is associated to plaque regression and stability of the plaque [8]. It is also worth mentioning that not all vulnerable plaques will rupture, but have only a high probability to rupture [9]. For example a vulnerable plaque can continue to growth due to intra-plaque bleeding, without rupture, resulting to total blockage of the lumen [9].

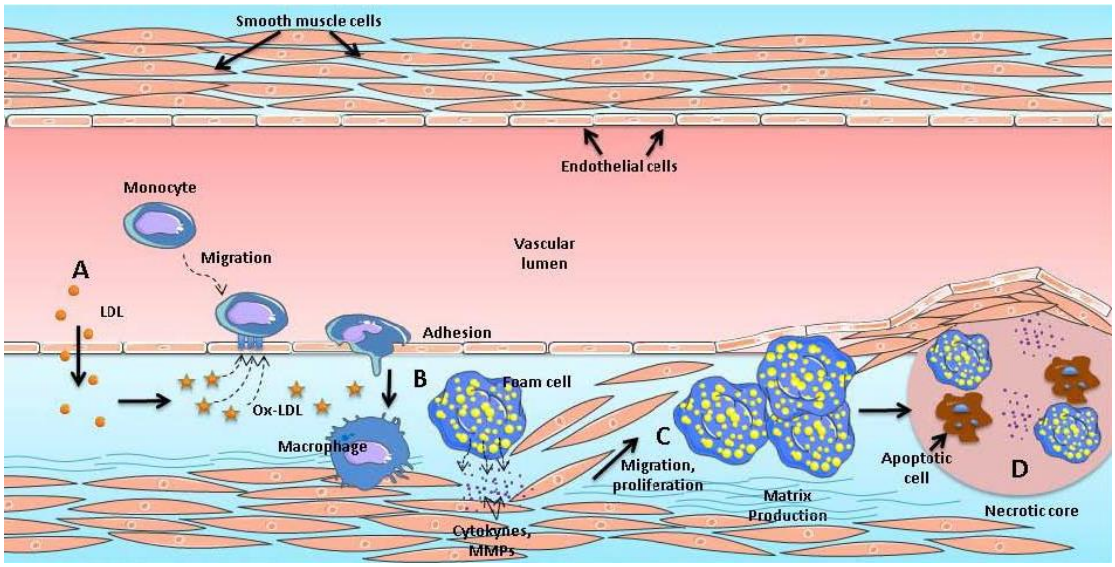

Figure 1: The building-up process of the plaque. **(A)** LDL from blood penetrates the endothelium and is introduced to the intimal layer where it is oxidized and triggers the inflammatory response. **(B)** Monocytes are being introduced to the vessel wall through the endothelium, where they differentiate into macrophages. They engulf oxidized LDL, which transforms them into foam cells. **(C)** Migration of vascular smooth muscle cells from media to intima. **(D)** The necrotic core. Figure received from [10].

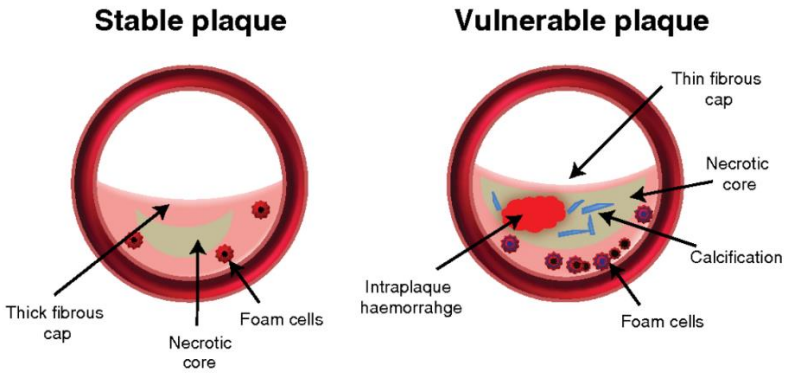

Figure 2: Examples of stable and vulnerable plaques. The plaque is the pink region that includes components such as necrotic core and foam cells. Although here it can be seen that the plaque size is the same in both cases, this is no always true. Figure received and adjusted from [11].

1.1. Imaging of the atherosclerotic plaque

In order to study the plaque in the arterial vessels, it is necessary to visualize it. This can be achieved by utilizing different image modalities. The two most frequently used catheter-based invasive image modalities in the coronary arteries are intravascular ultrasound (IVUS) and optical coherence tomography (OCT) [12], see Figure 3. The image modality IVUS utilizes the reflection of sound waves in order to provide image data. Information on plaque size can be provided through this technique and also it can detect calcifications, since their presence in the vessel wall blocks the signal [13] and thereby is visualized as a black shadow. However, IVUS is characterized by limited resolution (150 – 250 µm), which means that plaque components and cap thicknesses smaller than that resolution cannot be detected. On top of that it is unable to provide information about the lipids in the vessel wall [12], [14]. Despite

that, if IVUS is combined with signal analysis techniques that utilize the IVUS radiofrequency signal, it can provide information on the type of tissue. The most known example of this practice is the virtual histology IVUS (VH-IVUS) [15].

OCT is an image modality that utilizes the light that is emitted from a catheter and received back. It provides high resolution (15 – 20 μm) images, which enables the detection of small plaque structures such as thin caps [14]. Furthermore, the light waves can penetrate the calcifications which allow the visualization of the backside of the calcified regions and, on top of that, detection of lipids is also feasible [12]. However, the main disadvantage of this image modality is the limited depth of penetration; thus, there is no information regarding the plaque size.

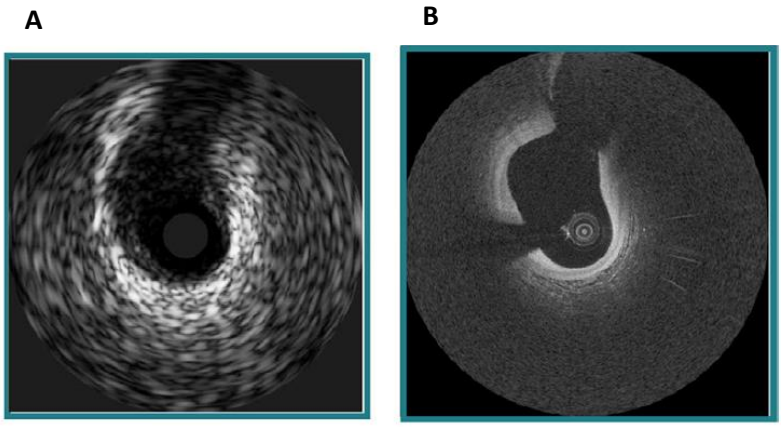

Figure 3: Cross-section of coronary artery. **(A)** Image based on intravascular ultrasound (IVUS). **(B)** Image based on optical coherence tomography (OCT). Figure received from [16].

1.2. Influence of biomechanics on atherosclerosis

Despite the fact that the formation of the atherosclerotic plaque is described by a cascade of specific events, the distribution of it is not uniform in the coronary arteries [17]. This non uniformity might be explained by the presence of local hemodynamic forces and the biomechanical stresses promoted by them. Thus, the biomechanical stresses might contribute to the formation and development of the plaque. On top of that, these forces may also influence the proneness of the plaque to rupture [18]. One of the local biomechanical forces that we are the most interested in is the blood flow induced wall shear stress (WSS) and is defined as the frictional force on the endothelium of the vessel wall. WSS is the result of the frictional force as a result of flowing blood along the vessel see Figure 4. It can be claimed that WSS is associated to the atherosclerosis since it has been related to processes that are connected to the atherosclerotic plaque formation, such as the regulation of the function of the endothelial cells [19], [20] and the vascular smooth muscle cells' death [21]. On top of that studies investigated the effect of WSS to the plaque progression. It was observed that at regions exposed to low WSS the plaque development was enhanced [22]–[24]. Furthermore, studies have reported enhanced plaque vulnerability when low or high WSS was acting at the endothelium [25]–[28].

During the cardiac contraction, the pulsating blood pressure applies a perpendicular force to the endothelial cells, see Figure 4. This pressure promotes expansion of the blood vessel wall. This type of deformation is named circumferential strain and the respective stress is called circumferential stress or cyclic stretch (CS). The circumferential stress that is located

inside an atherosclerotic plaque is also called plaque structural stress (PSS). The magnitude of plaque stress is associated with numerous parameters such as the size and the composition of the plaque and geometry of the lumen [29]. Studies have reported the contribution of PSS in plaque development. Tang et. al. suggested that low PSS may influence the plaque progression [30]. In a study of Liu et. al. they concluded that low PSS resulted in reduction of plaque volume [24]. However, high PSS lead to an increase in plaque size [23], [24]. Studies have also demonstrated that high PSS influence plaque phenotype and thereby promote plaque vulnerability, acute coronary syndrome and cardiovascular events [23], [31]–[35].

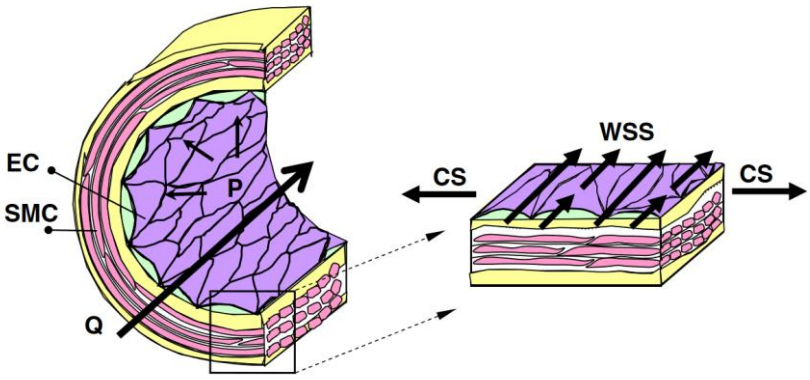

Figure 4: Transverse cross-section of a blood vessel along with the biomechanical stresses. Q is the blood flow, P is the pressure due to the blood flow Q and it is applied perpendicular to the endothelial cells (EC). SMC is an abbreviation of smooth muscle cells. On the right part of the figure the wall shear stress (WSS) and the circumferential stress (CS) are being displayed. Figure received from [36].

The number of studies that investigated the combined effect of WSS and PSS with respect to plaque progression are rather limited. The first study was a study performed by Tang et. al. in 2008. They observed that regions where the PSS and WSS were low, plaque progression was promoted and they stated that there might be an association between both low WSS and low PSS to plaque progression [30]. A more recent study was published by Costopoulos et. al. in 2019 [23]. They reported that high PSS combined with any level of WSS (low, medium or high) had an increasing effect in the necrotic core in area with plaque progression [23]. Thus, they stated that high PSS had an added effect to the wall shear stress [23].

The most important feature in this type of studies is the fibrous cap and its thickness, since it is the one shielding the necrotic core from being exposed to the blood flow and its thickness can affect the stresses [37], [38]. However, only thin caps are prone to rupture releasing the content of the necrotic core in the blood circulation [39]. Nevertheless, how thin should a fibrous cap be in order to be characterized as prone to rupture? Histopathological studies had provided an answer to that question by setting the threshold for thin caps at 65 μm [40], [41]. This indicates that in order to visualize these thin caps, image modalities with resolution equal or higher than this threshold must be utilized. Both those studies of Tang et. al. and Costopoulos et. al. utilized different image modalities to investigate the contribution of the combination of those stresses. Tang et. al. acquired their data from MRI [30], while Costopoulos et. al. used VH-IVUS [23]. However, these image modalities do not offer such high resolutions. Although, MRI has the potential to achieve high resolutions by increasing the strength of the magnetic field of the device, the writer did not find any study that fulfil this resolution criterion for studies in plaque progression in coronary arteries. Regarding the image modality VH-IVUS, its resolution varies between 150 – 250 μm, thus, it cannot detect thin cap

and microstructures [12], [14]. On top of that, there is not extensive histopathological validation of VH-IVUS plaque composition assessment [42]. One image modality that can overcome the aforementioned threshold is the OCT, which has resolution equal to 15 – 20 μm. However, OCT can provide information about the lumen and fibrous cap but not for the vessel wall. In order to overcome this limitation grayscale IVUS can be combined with OCT, since IVUS can provide information about the lumen and the vessel wall but not on the fibrous cap. By combining them a more detailed image can be constructed, using the advantages of each modality. Currently, no other studies were found that utilize the combination of OCT and IVUS in order to study the combined effect of WSS and PSS to the plaque progression in human coronary arteries.

1.3. Aim

Aim of this project was to investigate the contribution of the combination of WSS and PSS to the plaque progression of the human coronary arteries. This will be achieved by introducing a new methodology for the calculation of the stresses. This new methodology will utilize data from OCT and IVUS, an approach that will be used for the first time in this specific research topic.

Chapter 2: Methods

2.1. Participants

Data from patients with acute coronary syndrome (ACS) in hemodynamically stable condition admitted for percutaneous coronary intervention (PCI) were utilized in order to perform the stress calculations. The total number of participants were 48 and the total number of vessels that was imaged and utilized for this study was 49. Written informed consent was obtained from the participants. Approval of the study protocol was granted by the local medical ethical committee of Erasmus MC and the study was conducted in conformance with the World Medical Association Declaration of Helsinki (64th WMA General Assembly, Fortaleza, Brazil, October 2013) and Medical Research Involving Human Subjects Act (WMO). For more information about the participants and the inclusion and exclusion criteria see **Appendix A**.

2.2. Image acquisition protocol

The coronary segments were imaged utilizing OCT and NIRS-IVUS (TVC, InfraReDx (Burlington, Massachusetts, USA)). The targeted coronary segments contained at least two side branches and were at least 30 mm in length. The purpose of including side branches was to use them as matching points for co-registration of the OCT and IVUS images. Image acquisition of the participants was performed at two time points. The first time point is called T1 and is the baseline imaging. The second image acquisition performed after 12 months is called T2 and is the follow-up imaging.

2.3. IVUS analysis

The IVUS images were gated to obtain one frame per cardiac cycle in the same diastolic phase (acquired width 6 frames before the R-peak). For that purpose an algorithm that was developed in Erasmus MC was used. By applying that algorithm images at one moment of the cardiac cycle were selected and thereby lumen diameter changes because of cardiac contraction as well as due to non-linear catheter movement were removed. After completing the described process, the produced cross-sectional images were segmented by an experienced reader (Eline Hartman, MD) who utilized the software QCU-CMS software (Leiden, The Netherlands). In each of these images the lumen and external elastic lamina contours (a layer of connective tissue between media and adventitia) were delineated, see Figure 5A. Those contours were used in a later step. Regions with calcifications were excluded from the analysis since the ultrasound shadow (hypointense regions) created by them did not allow the tissue detection in these regions, see Figure 5B.

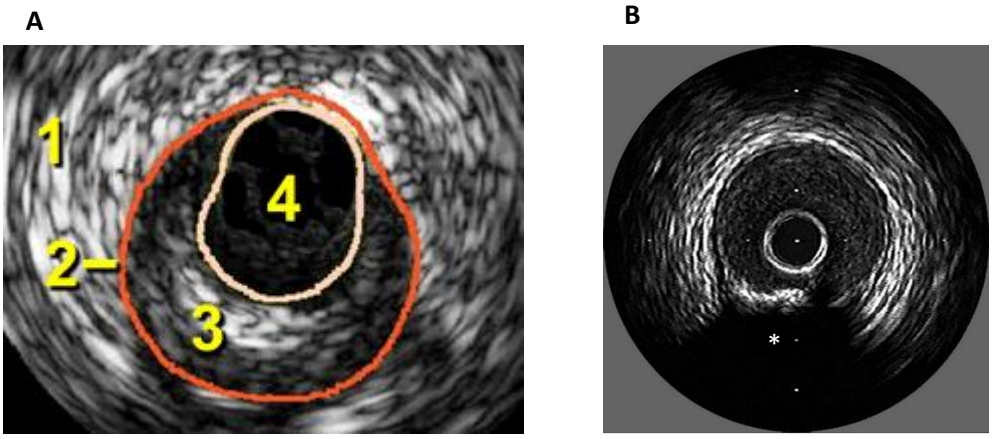

Figure 5: **(A)** IVUS cross-section depicting the contours. The number 1 depicts the adventitia. Number 2 is the media along with the external elastic lamina. Number 3 is the intima and number 4 is the lumen of the vessel. Figure received from [43]. **(B)** IVUS cross-section with calcification. The white asterisk (*) on the bottom side of the figure depicts a region with calcifications. Figure received and adapted from [44].

2.4. OCT analysis

The analysis of the OCT images conformed the consensus standards [45]. Assessment of plaque composition was performed every millimetre (1 out of every 5 frames). The plaque tissue components (fibrous tissue, lipid-rich plaque and lipid-pools) and their respective component angles from the lumen centre were identified manually. These tasks were performed by an experienced reader (Eline Hartman, MD). Since, we were interested in the regions with lipid-pools, also called necrotic cores (NC), only the identification of these regions will be described here. A region with necrotic core is visualized by OCT as a region with a sudden drop in signal, since lipids within the necrotic core absorb the emitted light preventing it from further penetration, see Figure 6. An overlying signal rich cap structure is present in Figure 6B. The cap structures and the lumen were delineated and utilized in a later step. The cap thickness for both time points T1 and T2 was calculated as the shortest distance between the cap and the lumen.

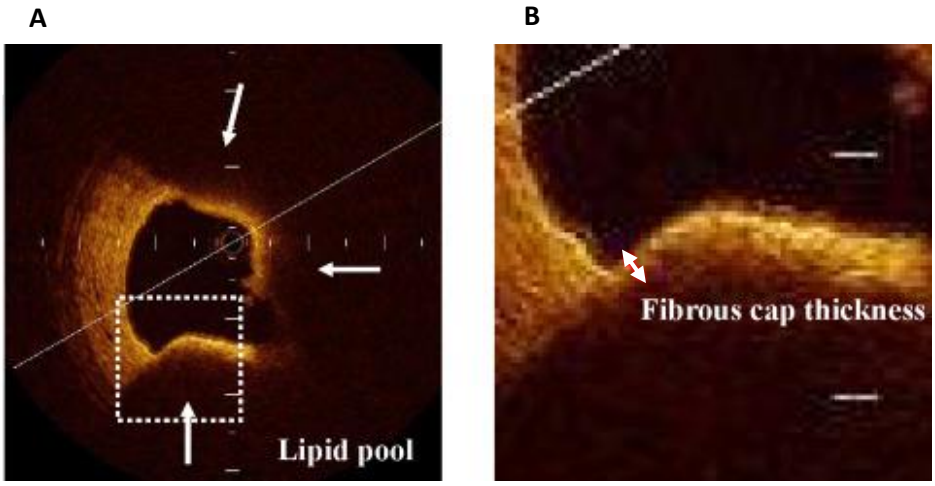

Figure 6: OCT cross-section with three lipid pools, also called necrotic cores. **(A)** The lipids absorb emitted light restricting further penetration; thus, there is a sudden signal drop. The white arrows depict the three lipid pools (necrotic cores). **(B)** The square of dot lines of Figure 4A enlarged. The thickness of region between the endothelium and the lipid pool (necrotic core) called fibrous cap thickness is visualized. Figure received from [46].

2.5. Geometry reconstruction and stress computation pipeline

Information obtained from OCT (location of necrotic core and fibrous cap) and IVUS (lumen and external elastic lamina), see Table 1, was used to create a 2D model of the atherosclerotic plaque and its composition. Subsequently this model was used to perform the stress calculations. Here, a brief overview of the pipeline that was developed, see Figure 7, will be provided and in later chapters each step will be explained in more details. The first step is the co-registration of the image data. Since, the image modalities OCT and IVUS were utilized, there was the need to fuse the data of them in order to create 2D cross-sections reconstructions of the imaged coronary plaques. However, since these 2D cross-sections will not contain all the necessary information – the contours of lumen, vessel wall and fibrous cap can only be extracted but not the contours of the necrotic core – there was the need to reconstruct the geometry of the necrotic core, see Table 1. For the reconstruction part of the necrotic core an algorithm that was developed in Erasmus MC was utilized [47]. After performing this step the produced cross-sections contained all the information required for the third step which is the calculation of the stresses in each cross-section.

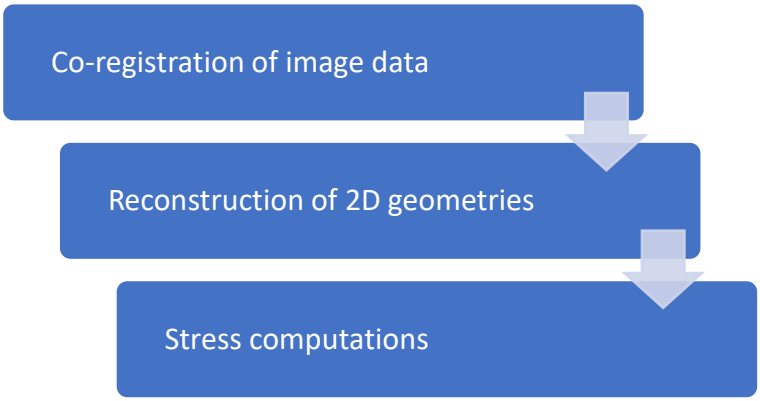

Figure 7: A block scheme of the three steps pipeline.

		Contours			
		Lumen	External elastic lamina	Fibrous cap	Necrotic core
Image modalities	IVUS	+	+	-	-
	OCT	+	-	+	-

Table 1: The image modalities OCT and IVUS and what information can be retrieved from them. The plus symbol (**+**) depicts that we can get that information from the specific image modality. The minus symbol (**-**) depicts that we lack that information from the specific image modality; thus, IVUS provides information about the contours of the lumen and the external elastic lamina, but there is no information about the fibrous cap and the necrotic core. The OCT image modality can only provide information about the contours of the lumen and the fibrous cap. However, in this study the lumen contours from the OCT were not utilized. It is clear that none of them can provide information about the necrotic core; thus, there is the need to reconstruct it.

2.5.1. Step 1: Co-registration of image data

The first step was to register the data from the two different image modalities. As it was mentioned before in this document, during the imaging at least two side branches were imaged. Those side branches were utilized as reference points for the co-registration of the OCT and IVUS. The co-registration is performed in two steps. The first step is the longitudinal co-registration, see Figure 8C. At that step the OCT and IVUS segments were matched based on the branch location. When the longitudinal co-registration was completed, then the OCT and IVUS segments were registered in the circumferential direction, see Figure 8D. Circumferential co-registration is performed at the side branches that were identified as reference points. During the registration the IVUS image is fixed and a rotation is applied to the registered OCT image in order to match each other circumferentially. For the cross-sections between the two side branches (reference points) linear interpolation of the rotation was performed. Both the longitudinal and circumferential co-registration were performed manually.

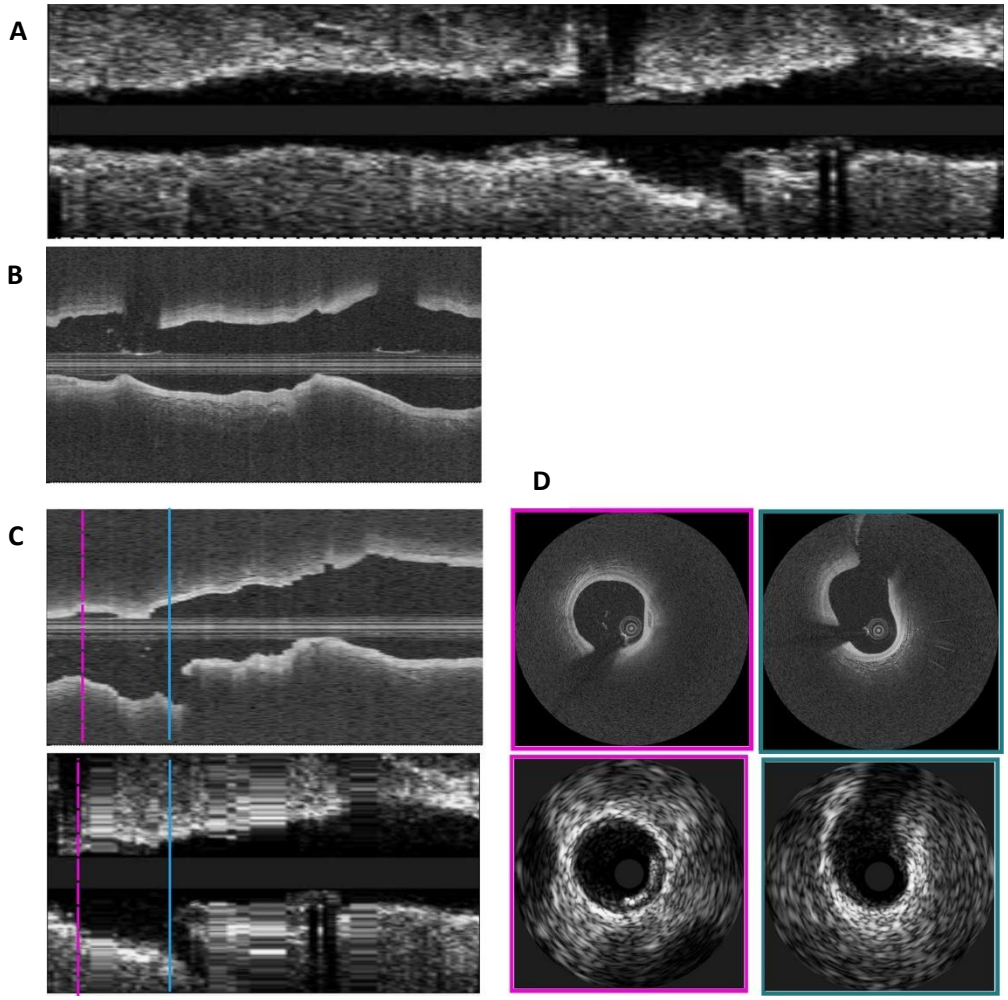

Figure 8: Example of co-registration of OCT and IVUS. **(A)** Example of IVUS in longitudinal view before co-registration. **(B)** Example of OCT in longitudinal view before co-registration. **(C)** Longitudinal co-registration of IVUS and OCT images. **(D)** Circumferential co-registration of IVUS and OCT images. Figure received from [16].

2.5.2. Step 2: Reconstruction of 2D geometries

The basis of the 2D reconstruction is the lumen and the external elastic lamina delineated from the IVUS. After performing the matching of OCT and IVUS, the fibrous caps that were identified in the OCT images were mapped to their matched IVUS images. The mapping of the cap was performed by calculating first the cap thickness based on OCT (this is the shortest distance between the cap and the lumen). The cap thickness was then projected as distance from the lumen at the matched location in the IVUS image. In Figure 9 there are two examples, one case without cap (Figure 9A) and one case with one cap (Figure 9B). As it can be seen in Figure 9B the geometry consists of the lumen, the external elastic lamina and the cap. However, there is no information about the size of the necrotic core that is shielded by the cap. Subsequently, this incomplete 2D geometry was used as input for the reconstruction of the necrotic core, which was the next step.

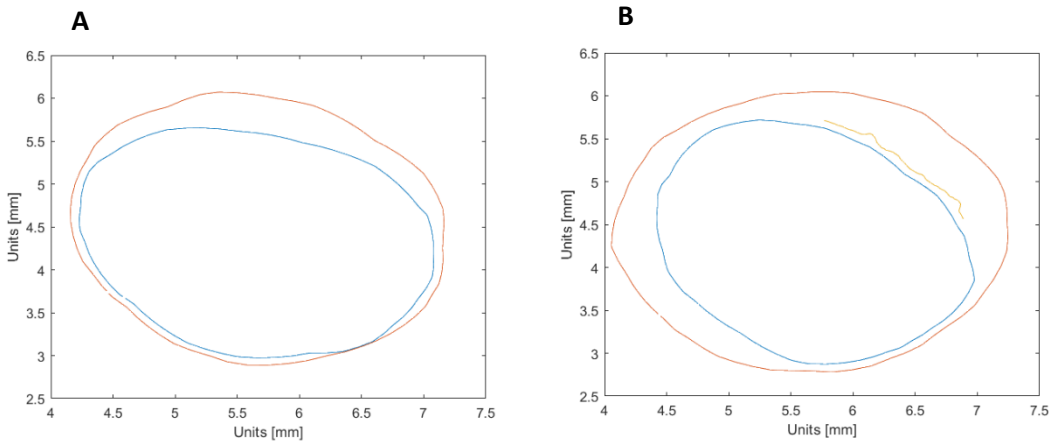

Figure 9: Incomplete 2D geometries **(A)** with no cap. **(B)** with one cap. The red colour is the external elastic lamina contours from IVUS, the blue depicts the lumen contours received from IVUS and the yellow the cap contours received from OCT.

In order to obtain a complete 2D geometry, the backside of the necrotic core needs to be constructed. For that part an algorithm, which was developed in the Biomechanics lab (Biomedical Engineering, Cardiology, Erasmus Medical Center, Rotterdam), was used [47]. In that study, it was shown that the geometry and the stress calculations of the ground truth, i.e. histological data, and the geometry based on the reconstruction approach are in good agreement. For the reconstruction of the backside of the necrotic core, the necrotic core thickness was estimated at three locations. There was one estimation at the centre of the necrotic core (50%), midcap, one at the side of the necrotic core, i.e. 25% of the total angle of the necrotic core and one at the other side, i.e. at 75% of it, see Figure 10; these were called sidecaps. The following equation was used for the different locations as described by Kok. et. al. [47]:

$$rNCt_i = \beta_{0,i} + \beta_{NC\ angle,i} \cdot (LP\ angle\ [rad]) + \beta_{IMT,i} \cdot (IMT\ [\mu m]) + \\ + \beta_{capT,i} \cdot (capT\ [\mu m]) \quad (1)$$

where i indicates the midcap (50%) or the sidecaps (25% and 75%), the $rNCt_i$ is called the relative thickness of the necrotic core since it is relative to the wall thickness and it is the estimation of the thickness of the necrotic core for the midcap or the sidecaps. In this algorithm the cap thickness ($capT$), the angle of the necrotic core ($NC\ angle$) and the intima – media thickness (IMT) were used. The cap thickness, as well as the angle of the necrotic core were retrieved from OCT. The intima – media thickness was based on the distance between the lumen and vessel wall, that were retrieved from IVUS. For the parameters of the equation (1) $(\beta_{0,i},\ \beta_{NC\ angle,i},\ \beta_{IMT,i}$ and $\beta_{capT,i})$ the mean value of each one, reported in table 2 of [47], was used. A replication of that table can be seen in Table 2 below.

	β_0	$\beta_{NC\ angle}$	β_{IMT}	β_{capT}
$rNCt_{midcap}$	187 ± 55.4	63.3 ± 26.6	0.29 ± 0.07	-0.51 ± 0.08
$rNCt_{\pm sidecap}$	175 ± 46.4	130 ± 19.8	0.18 ± 0.05	-0.42 ± 0.06

Table 2: The range of values of the parameters of the model described by the equation (1). This table is a replication of the table 2 in [47].

The equation (1) will give us three points, the thickness of the necrotic core at midcap (50%) and at the two sidecaps (25% and 75%). Those three points will be used to reconstruct the backside of the necrotic core, see Figure 10; however, the two edges of necrotic core should also be reconstructed.

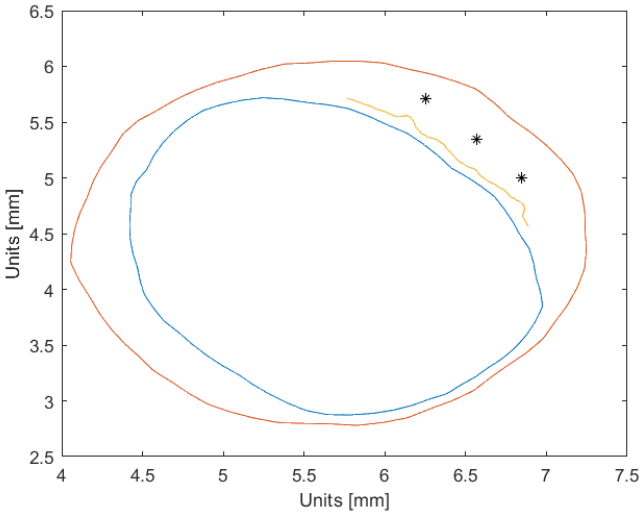

Figure 10: A cross – section after the solution of equation (1). The red colour is the external elastic lamina, the blue depicts the lumen and the yellow the cap. The black marks indicate the midcap and the two sidecaps.

For the reconstruction of the edges of the necrotic core, the same principle as presented in [47] was used. Since the writer observed that the edges of the necrotic core display rounded features, for the creation of each side of the necrotic core a circular arc was used. Other than the published approach, the radius of the arc was calculated based on the relative necrotic core thickness of the midcap ($rNCt_{50\%}$) and the sidecaps ($rNCt_{25\%}$ and $rNCt_{75\%}$), as it can be seen in equation (2).

$$radius = \frac{rNCt_{25\%} + rNCt_{50\%} + rNCt_{75\%}}{3} \quad (2)$$

Parabolic fitting was used to connect the points on the backside of the necrotic core, black asterisks on Figure 10, and the parts of the circles that form the sides of the necrotic core. In Figure 11 two examples of plaques are being displayed, one without and one with a necrotic core. During data processing, also an extra tissue component is added to the geometry surrounding the plaque and is named a buffer. The purpose of this component will be explained in next chapter.

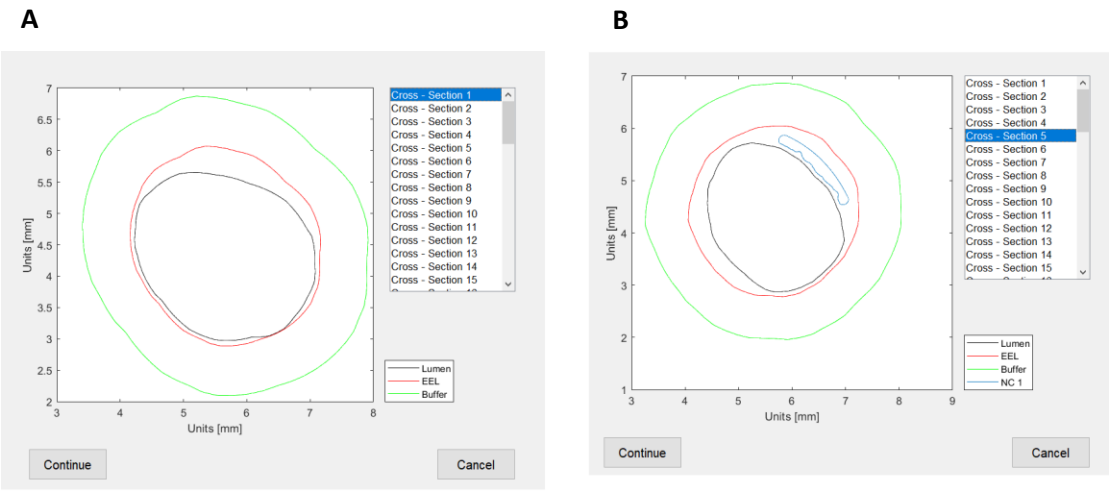

Figure 11: Complete 2D geometries. **(A)** A 2D geometry with no necrotic core. **(B)** A 2D geometry with one necrotic core.

2.5.3. Step 3: Stress computations

For the stress calculations finite element analysis (FEA) was utilized. In order to perform this analysis the 2D plaque geometries were transferred into ABAQUS (version 6.13, Dassault Systemes Simulia Corp., Providence, RI, USA). The geometries were imported through a script that was developed in Python. In ABAQUS the geometry was prepared for the stress calculations. This was achieved by performing a few actions. Firstly, the boundary condition was defined. Afterwards, the material of each components was defined, as well as the type of the element. Lastly, the geometry was meshed.

The complete 2D geometries from the **Step 2: Reconstruction of 2D geometries** had one component called buffer, see Figure 11. The purpose of this segment was to limit the rigid body motion during the finite element analysis. On the outer edge of the buffer a boundary condition was set preventing the displacement and the rotation of it.

Regarding the material of the components, all of them were assumed isotropic. The neo – Hookean hyperelastic material model was utilized also for all of them, which was also used in earlier studies [48]–[50]. The equation that describes that model is the following:

$$W = C_{10}(I_1 - 3) + \frac{1}{D_1}(J_{\mathrm{el}} - 1)^2 \tag{3}$$

where W is the strain energy density function, C_{10} denotes half of the shear modulus, I_1 is the first invariant of the right Cauchy – Green deformation tensor, D_1 enforces the compressibility of the material in the computations and J_{el} represents the elastic volume strain. For the material properties C_{10} and D_1 the values presented in the paper published by Kok et al. [47] were used; however, those values and their references from where they were retrieved will also be presented here in the Table 3. The intima and the necrotic were assumed almost complete incompressible ($D_1 = 1\mathrm{e} - 5\ \mathrm{kPa}^{-1}$).

Material	C_{10} [kPa]	D_1 [kPa^{-1}]	Reference
Intima	166.7	1e-5	[51]
Necrotic core	1	1e-5	[52]
Buffer	10	0.02	[53]

Table 3: The components, their material properties and the references from where the values were retrieved. This table is a replication of the table 1 in [47].

The element shape was triangular and the plane strain element CPE3H (3-node linear, hybrid with constant pressure) was utilized. The term "3-node linear" depicts that each element consists of 3 nodes and is characterized by linear deformation. The term "hybrid" depicts that the volume of the element cannot change when pressure is applied. The term "constant pressure" indicates that the pressure is modeled as a constant throughout the entire element. Each component had a number of nodes that can vary slightly depending the overall size of the geometry. The intima had about 5200 nodes, the necrotic core had about 970 nodes, while the buffer had around 9600 nodes. Intima consisted of about 9400 elements, the necrotic core had about 1700 elements and the buffer had about 18500 elements.

When the geometry was meshed, it was subdivided into smaller domains called elements. On those elements the equations for the calculation of the stresses were solved. The stresses were calculated in the ABAQUS based on the force and momentum equilibrium equations and the metric that was used as output was von Mises stress. Thus, PSS was defined as the von Mises stress produced by the perpendicular application of pressure to the peri-luminal region. For the analysis, however, each cross-section is divided in eight sectors with a 45° angle width. The centre of lumen of each cross-section was used in order to create the sectors. An example can be seen in Figure 12. Each sector had a stress value which was the average of the stress values of the peri-luminal region contained in that sector. The whole lumen was consisting of 360 nodes out of the total nodes that intima had. Each of those 360 nodes was representing 1° (one node of the lumen = 1°, so the 360 nodes of the lumen = 360°) and each one of those had a stress value. Thus, the stress value for each sector was the mean PSS of the 45 corresponding nodes of the lumen region.

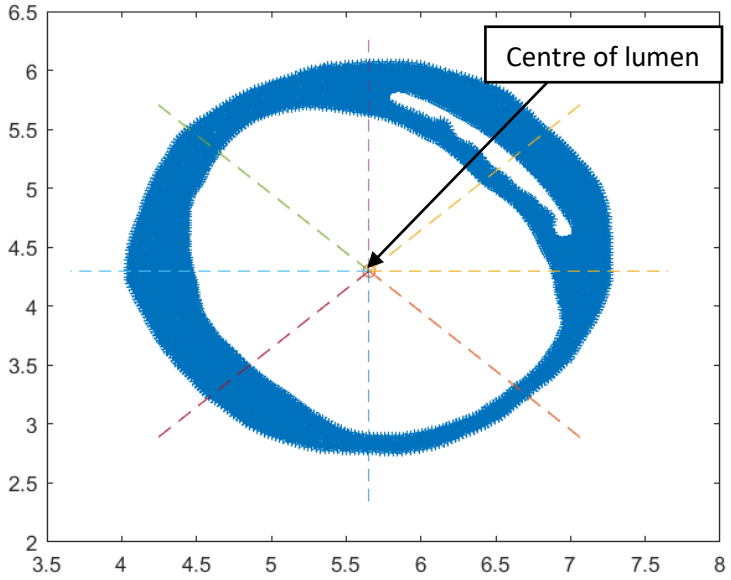

Figure 12: Example of division of a cross-section in eight sectors.

The coronary arteries are under pressure during imaging, This means that the initial state is not stress-free. Thus, these initial stresses need to be calculated [50]. This can be achieved by utilizing the Backward Incremental method [50]. For more information regarding the Backward Incremental method see **Appendix B**. By implementing this method, a pressure equal to 80 mmHg is applied to obtain initial stresses. Subsequently, an increment of a 40 mmHg pressure was applied as the loading condition, which represents the systolic blood pressure.

2.6. Calculation of wall shear stress

WSS is a vascular mechanical force related to the blood flow, see Figure 4. The calculations of the wall shear stresses were not performed by the writer of this document. However, in this section some fundamental information is provided.

For the calculation of the WSS the computational fluid dynamics software mFluent (ANSYS Inc., Canonsburg, PA, USA) was utilized. The fluid domains were discretized in ICEM CFD (ANSYS in., USA) by means of tetrahedrons. The total number of elements was six million. The blood was assumed to be homogeneous and incompressible. Its density was equal to $1060\ \frac{kg}{m^3}$ $\left(\rho = 1060\ \frac{kg}{m^3}\right)$. The gravity load was neglected. The vessel wall was characterized by rigidity and there was no slip. The Navier-Stokes equation was used for the calculations. Although the discrete form was solved numerically, the continuous form is presented in the equation (4).

$$\frac{\partial \boldsymbol{u}}{\partial t} + \boldsymbol{u} \cdot \nabla \boldsymbol{u} = -\frac{\nabla P}{\rho} + \upsilon \nabla^2 \boldsymbol{u} \tag{4}$$

where $\boldsymbol{u}$ depicts the fluid velocity vector, P is the fluid pressure, ρ is equal to $1060\ \frac{kg}{m^3}$ $\left(\rho = 1060\ \frac{kg}{m^3}\right)$ and is the fluid density and υ depicts the kinematic viscosity.

For the calculation of the magnitude of WSS in blood vessels the time-average value (TAWSS) over one cardiac cycle is utilized. For the calculation of it the following equation was used:

$$TAWSS = \frac{1}{T}\int_0^T |\boldsymbol{\tau_{wss}}|\, dt \tag{5}$$

$\boldsymbol{\tau_{wss}}$ is the WSS vector and T is dependent on the heart rate and is the period of one cardiac contraction.

2.7. Statistical analysis

First of all, there were cross-sections with calcifications. Those cross-sections were removed, as calcifications can affect the stress calculations and wall thickness cannot be assessed accurately in those regions. Furthermore, the change in wall thickness between the time points T1 and T2 was used as metric for the plaque progression. Each sector had two wall thickness values, one for time point T1 and one for time point T2. The wall thickness of each sector was the average over the wall thickness of the respective region and respective time point. For the calculation of the change in wall thickness for each sector of each cross-section the following equation was used:

$$\Delta WT_{j,i} = WT_{T2,j,i} - WT_{T1,j,i} \text{ with } j = 1, \dots, N \text{ and } i = 1, \dots, 8 \quad (5)$$

where j depicts the studied cross-section, N is the total number of the cross-sections, i depicts the studied sector of the cross-section, $WT_{T1,j,i}$ is the average wall thickness of the sector i of the cross-section j at the time point T1, $WT_{T2,j,i}$ is the average wall thickness of the sector i of the cross-section j at the time point T2 and $\Delta WT_{j,i}$ depicts the change in wall thickness between the time points T1 and T2 of the sector i of the cross-section j.

Both PSS and WSS were divided into three categories (low, 0 – 33.3th percentile, medium, 33.4 – 66.6th percentile, high, 66.7 – 100th percentile). Two different types of data division were studied here. The first approach is called vessel specific. This means that the data of each vessel were divided into the three aforementioned ranks based on threshold values of the studied vessel and so, for each vessel the range of those categories was different. The second approach was based on absolute thresholds. In this case the aforementioned ranking was based on threshold values of the whole sample size not taking into account if the sectors are from the same vessel or not. Those two different approaches were studied in order to explore also if the vessels respond to the absolute values of biomechanical stresses or it is relative to their respective biomechanical stresses.

In order to check the effect of WSS, PSS and their combination on the change of wall thickness, the statistical method ANOVA with Bonferroni post-hoc testing was implemented, therefore change in wall thickness, $\Delta WT_{j,i}$, was assigned as dependent variable. The independent variables were the PSS and / or WSS and they were defined as low, medium or high as described previously. The identifier of the vessel was introduced as a random factor, since there are multiple observations (cross-sections) per vessel and they may not be independent. Apart from that, the wall thickness at time point T1 was also included in the model as covariate. By doing so, we account for possible “regression to the mean” effects. Regression to the mean can occur when the measured variable has an extreme value on the first measurement, while the value of the second measure is lower than the first one and closer to mean. The “regression to mean” effects can introduce errors; thus, there it was needed to take those effects into account. As outcome of the model the estimated means of the change in wall thickness was calculated for the sectors exposed to low, medium and high WSS or PSS. In addition we checked if there was a synergistic or additive effect of PSS and WSS on plaque progression. For the statistical analysis the software IBM SPSS Statistics for Windows was used (version 25, IBM Corp., Armonk, N.Y., USA). The graphs that are presented in the **Chapter 3: Results** describe the mean effect of the studied case, while the error bars are equal to two times the standard error ($mean - 2 \cdot std_{error}$ and $mean + 2 \cdot std_{error}$). The values of PSS and WSS were also checked for normality. Lastly, $p < 0.05$ is considered statistically significant.

Chapter 3: Results

The number of the participants was 48 and the total number of the imaged vessels was 49. The initial number of the cross-sections was 2485. From those cross-sections 18 were excluded because the backside of the necrotic core was intersecting the front side of it, see **Chapter 6: Limitations**. Moreover, there were 4 cross-sections that the lumen of the OCT and IVUS did not have the same shape. Those cases were also excluded. On top of that, the cross-sections with calcifications were also removed; thus, the total number of cross-sections used in this study was 1042 (21.3 ± 13.5 cross-sections per vessel). The total number of sectors was 8328. It needs to be mention that the total number of sectors were slightly less than the expected one ($1042 \cdot 8 = 8336 > 8328$). This was happening because there was a small number of sectors with bifurcations. Those sectors were removed resulting to a total number of 8328 sectors instead of 8336. Regarding the PSS in Figure 13 two examples of cross-sections with stress distribution are provided. In Figure 13A there is a cross-section with one necrotic core, while in Figure 13B there is one cross-section without necrotic core. On both figures the buffer, the lumen and the region between the lumen and the external elastic lamina are visualized. On the left side of each figure there is a colourbar depicting the range of the PSS in kPa for each respective cross-section. It can be seen that there is an inverse relationship between the wall thickness and the PSS. The peak value of the PSS in Figure 13A was observed close to the lumen at the region with the smallest wall thickness and it was equal to 135.2 kPa. The PSS at the region of the fibrous cap ranged from 45.18 kPa to 78.94 kPa. For the Figure 13B the peak value was 90.3 kPa and it was located close to the lumen.

Both PSS and WSS were not normally distributed. The median of the PSS was equal to 51.03 kPa, while the 25th percentile was equal to 40.6 kPa and 75th percentile was equal to 66.1 kPa. For the WSS the median value was 0.9 Pa, the 25th percentile was 0.5 Pa and the 75th percentile was 1.6 Pa.

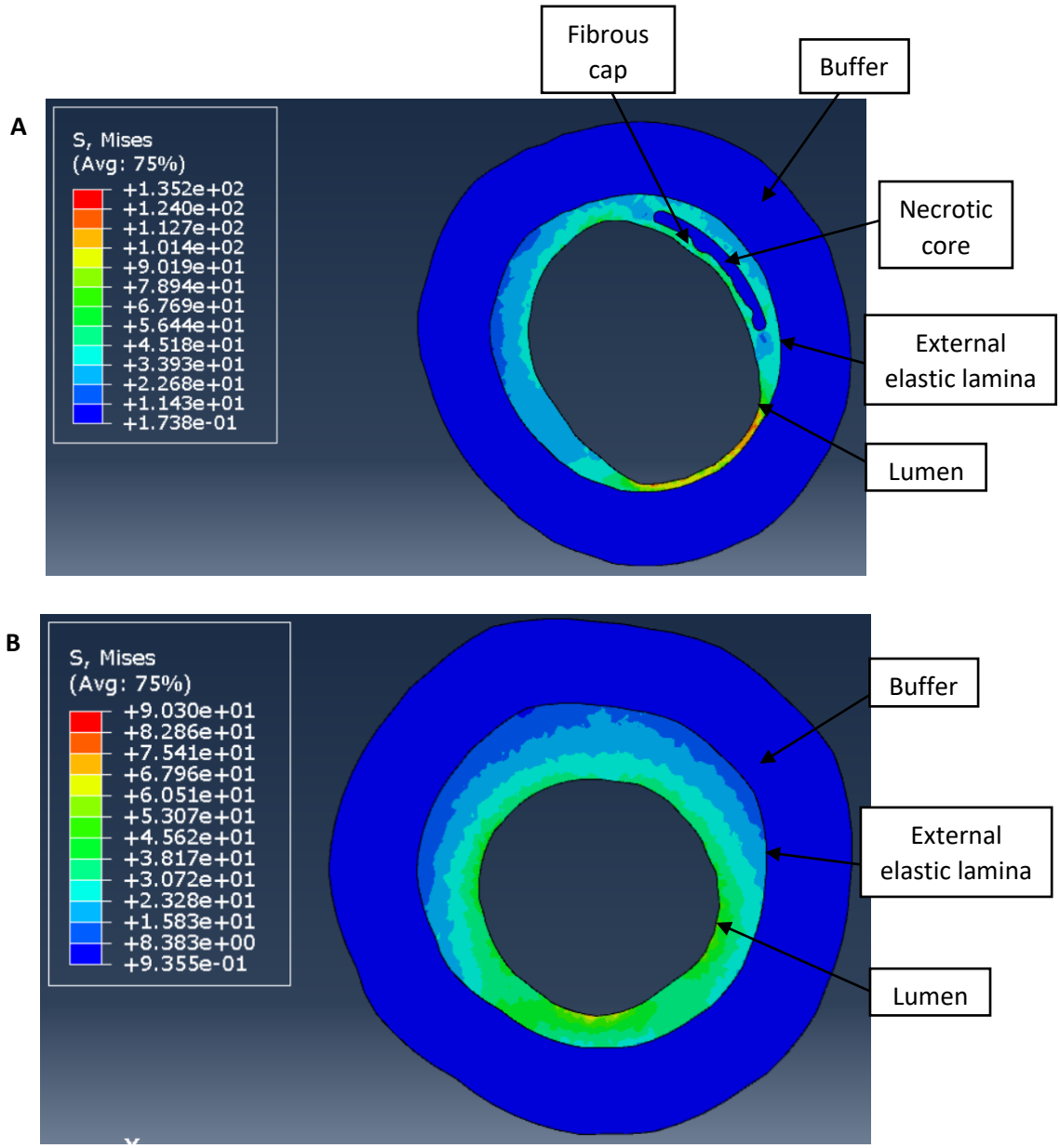

Figure 13: Complete 2D geometries and their components after stress calculations in ABAQUS. On the left side of each cross-section there is the respective colourbar for the PSS in kPa. **(A)** A 2D geometry with necrotic core. **(B)** A 2D geometry with no necrotic core.

3.1. Vessel specific analysis

3.1.1. Association of PSS and changes in wall thickness

In Figure 14 the change in wall thickness with respect the three levels of PSS is depicted. It was observed that PSS has not a statistically significant effect on plaque progression ($p = 0.137$). This indicates that plaque growth (as measured with wall thickness change) is not associated with PSS. In the Table 11 in **Appendix C** the mean values and the standard errors are being presented.

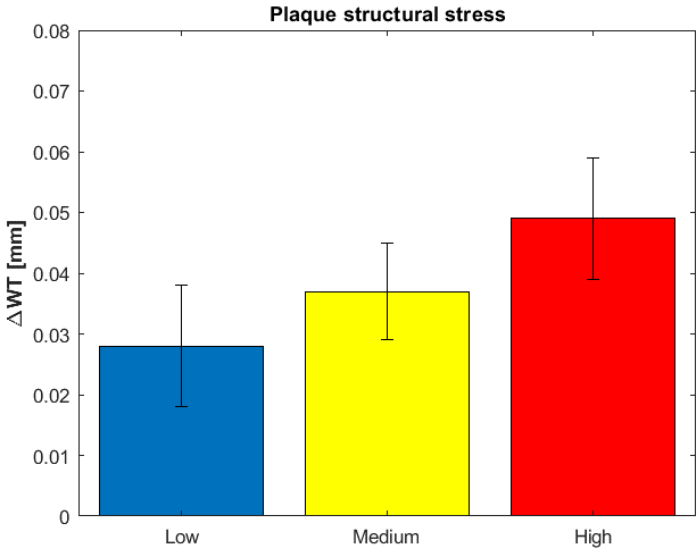

Figure 14: PSS with respect to the change in wall thickness.

3.1.2. Association of WSS and changes in wall thickness

In Figure 15, the effect of WSS to the change in wall thickness is visualized. From the statistical analysis of WSS, it was demonstrated that WSS has a statistical significant effect on plaque progression ($p < 0.0001$). It can be seen that the lower the WSS is, the greater the wall thickness increment is. It is visible that plaque progression was statistically different for the sectors exposed to low WSS compared to those exposed to high WSS. Furthermore, the statistical significant was the difference also to the sectors where low WSS is applied compared to the sectors exposed to medium WSS. The pairwise comparisons between them is presented in the Table 4, while in the Table 12 in **Appendix C** the mean values and the standard errors are being presented. It can be noticed in this case that for low WSS there is plaque progression.

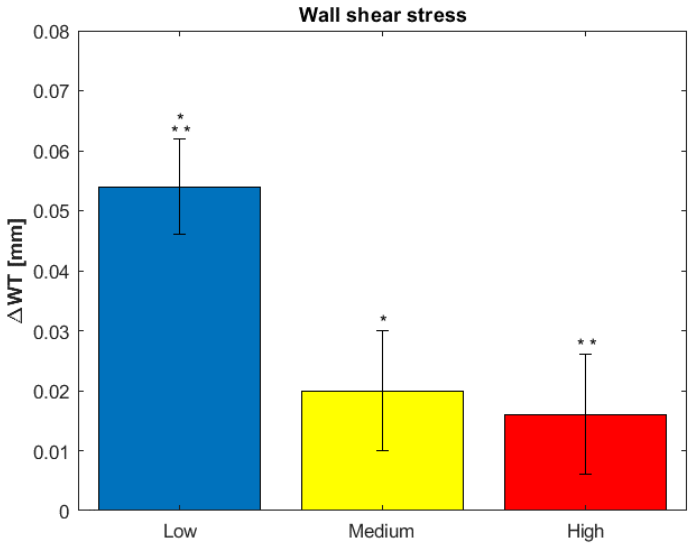

Figure 15: Association of the WSS and the change in wall thickness. The asterisk (*) indicates statistical significance ($p < 0.05$) between low and medium WSS, while the double asterisk (**) depicts statistical significance ($p < 0.05$) between low and high WSS.

Pairwise comparison			
WSS combinations	**Statistical significance**	**Confidence Interval**	
		Lower bound	**Upper bound**
Low – Medium	< 0.0001	0.019	0.049
Low – High	< 0.0001	0.023	0.054
Medium – High	1	- 0.012	0.022

Table 4: Pairwise comparison of the three categories of WSS.

3.1.3. Association of changes in wall thickness and the combination of WSS and PSS

The contribution of the combination of PSS and WSS to the change of wall thickness is visualized in Figures 16. In this combined analysis the PSS has not a statistically significant effect ($p = 0.280$) on plaque progression, while WSS has a statistically significant effect ($p < 0.0001$). It is visible that sectors exposed to low WSS demonstrated the greatest plaque development. Overall, PSS did not contribute to plaque progression; thus the plaque development is entirely estimated by WSS. In **Appendix C** there is the Table 13 with the mean values and the standard errors.

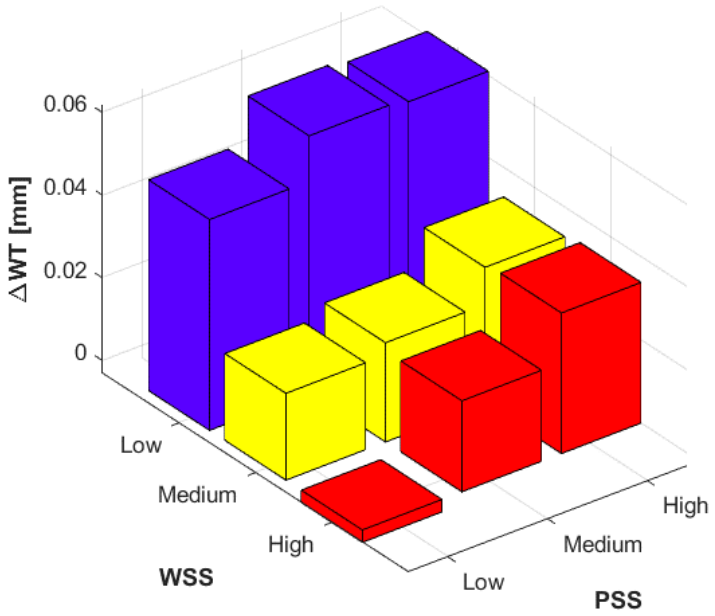

Figure 16: 3D visualization of the effect of the combination of WSS and PSS on the change in wall thickness. Only the mean values are being displayed.

Pairwise comparison			
WSS combinations	**Statistical significance**	**Confidence Interval**	
		Lower bound	**Upper bound**
Low – Medium	< 0.0001	0.015	0.047
Low – High	< 0.0001	0.023	0.058
Medium – High	0.743	- 0.010	0.028

Table 5: Pairwise comparison of the three categories for the combined analysis.

3.2. Analysis based on absolute thresholds

3.2.1. Association of PSS and changes in wall thickness

In Figure 17 the effect of the PSS to the wall thickness change based on absolute thresholds is presented. PSS had a borderline statistically significant effect (p = 0.091); on plaque progression. As it can be seen in Figure 17, the greatest increment in wall thickness is observed for the case of high PSS. In the Table 14 in **Appendix C** the mean values and the standard errors are being presented.

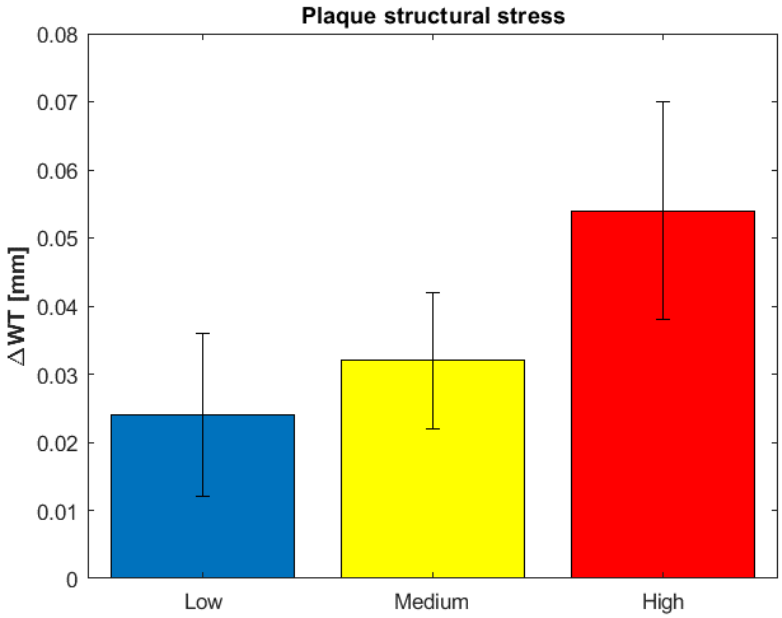

Figure 17: Association of the PSS and the change in wall thickness.

3.2.2. Association of WSS and changes in wall thickness

In Figure 18, the effect of WSS on the change in wall thickness is visualized. In this case it was observed that WSS has a statistically significant effect on plaque progression (p = 0.004). Furthermore, there was a statistically significant difference in plaque progression between the cases of low and medium WSS (p = 0.002). The pairwise comparisons between the them is presented in the Table 6, while in the Table 15 in **Appendix C** the mean values and the standard errors are being presented. It is visible in this case that low WSS can greatly promote wall thickness progression.

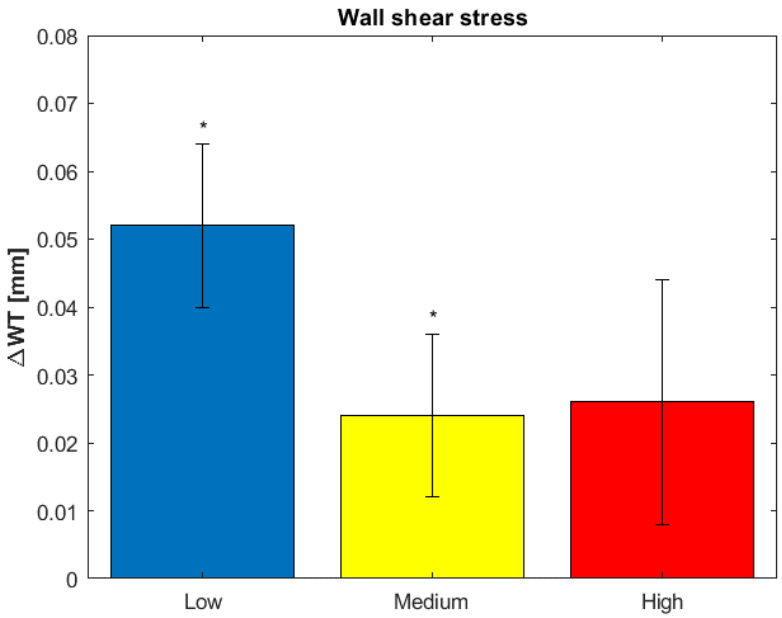

Figure 18: Association of the WSS and the change in wall thickness. The asterisk (*) indicates statistical significance ($p < 0.05$) between low and medium WSS.

Pairwise comparison			
WSS combinations	**Statistical significance**	**Confidence Interval**	
		Lower bound	**Upper bound**
Low – Medium	0.002	0.008	0.048
Low – High	0.060	- 0.001	0.053
Medium – High	1	- 0.028	0.024

Table 6: Pairwise comparison of the three categories of WSS.

3.2.3. Association of changes in wall thickness and the combination of WSS and PSS

In Figure 19 a 3D graph visualise the effect of the combination of the biomechanical stresses. In this case PSS was not statistical significant ($p = 0.117$), and WSS had only a borderline significant effect ($p = 0.064$) on plaque progression. In the **Appendix C** the mean values and the standard errors are being presented in the Table 16. From the Figure 19 it is visible that the combination of high PSS with high WSS might promote plaque development, however there was no statistical significant effect.

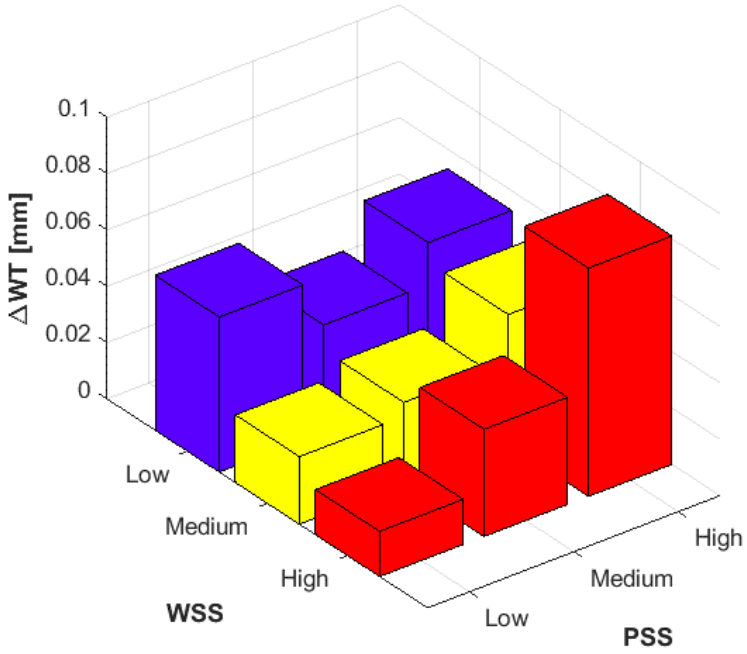

Figure 19: 3D visualization of the effect of the combination of PSS and WSS on the change in wall thickness. The statistical significance between the different cases and the error of each case is not displayed. Only the mean values are being displayed.

Chapter 4: Discussion

In this study for the first time OCT and IVUS are utilized in order to investigate the link between the plaque progression and the combination of PSS and WSS. Regarding the individual effect of PSS, the wall thickness was being increased at sectors exposed to high PSS. However, its effect was not statistically significant. The individual effect of WSS was statistically significant and it was observed that there was plaque development at sectors exposed to low WSS. From the analysis of the combined biomechanical stresses it was demonstrated that when low WSS was combined with any level of PSS the plaque development was greatly enhanced for the vessel specific case. However, only WSS had a statistical significant effect to plaque progression, while PSS had not. Thus, WSS was entirely responsible for plaque development. Regarding the combined effect of the biomechanical stresses for the approach of absolute thresholds the combination of high PSS with high WSS might enhance plaque development but neither PSS nor WSS were statistically significant.

From those types of data division, it is believed by the writer that the vessel specific is more valid. The justification of this statement is that the patients are different between each other and, thus, the blood vessels. So, in vessels of different patients, the biomechanical stresses are different and the three levels, low, medium and high, can have different ranges for each vessel. However, what was the differences in ranking between those two approaches? The answer to that questions is depicted to the Table 7 and Table 8. In those tables the distribution and the differences of the data between those two approaches are depicted. For example, in Table 7 from all the data the 26.11% were ranked as low for both the approaches. The 7.21% were ranked as low in the vessel specific approach and medium in the approach of the absolute thresholds and so on. If the percentages in Table 7 are summed, the result will be 100% depicting the total number of data (sectors) used in this study. The

same logic applies also in the Table 8. In the literature both types of data division were utilized. In the more recent study on that topic Costopoulos et. al. used the absolute thresholds ranking [23], while Lie et. al. implemented the vessel specific ranking [24].

Plaque structural stress

		Absolute thresholds		
		Low	**Medium**	**High**
Vessel specific	**Low**	26.11%	7.21%	0.02%
	Medium	7.01%	19.89%	6.44%
	High	0.22%	6.22%	26.88%

Table 7: Distribution of the data for PSS are presented.

Wall shear stress

		Absolute thresholds		
		Low	**Medium**	**High**
Vessel specific	**Low**	23.55%	12.22%	2.43%
	Medium	7.76%	14.37%	12.3%
	High	2.03%	6.72%	18.62%

Table 8: Distribution of the data for the WSS are presented.

Regarding the results, the range of the values of PSS and WSS were similar to those previously reported in figures or graphs in the literature [24], [30]. Regarding the individual effect of PSS Tang et. al. reported that the PSS correlates negatively with the plaque formation in the carotid arteries [30]. Liu et. al. studied the connection between the PSS and plaque progression. They observed that PSS had a statistical significant effect to the change of plaque volume [24]. They also reported that high PSS enhanced the plaque volume, while for low PSS the plaque volume was reduced [24]. Similar observations were reported by Costopoulos et. al., who demonstrated that high PSS increment in the necrotic core and reduction of it for the case of low PSS [23]. We noticed the same trend that with increasing the PSS the wall thickness change increased. However, in contrast to Costopoulos, we did not notice a reduction in wall thickness for sectors exposed to low PSS. Moreover, no statistically significant contribution of the PSS to plaque progression was observed.

Regarding the WSS it was demonstrated here that low WSS promotes the increment in wall thickness; thus, enhanced the plaque development, a result consisted with other

studies [22], [23], [30]. Liu et. al. also demonstrated an increment in plaque volume for the case of low WSS; However, the effect in their study was not statistical significant [24].

Tang et. al. reported in their study that regions where low PSS was combined with low WSS there was plaque progression [30]. Here we observed that for the combination of WSS and PSS for the vessel specific approach the PSS did not contribute to plaque progression. The plaque progression was entirely estimated by WSS and only at sectors exposed to low WSS plaque progression was promoted. Costopoulos et. al. reported that in areas of progression WSS (low, medium or high) combined with high plaque structural stress can enhance plaque development [23]. In the vessel specific approach those combinations had not such an increment effect as the combinations of low WSS with any level of PSS. However, despite those trends, it should be taken into account that for the approach of vessel specific those trends could be entirely described from the WSS since no statistical significance was observed for the PSS. In the approach of absolute thresholds the combination of high PSS and high WSS might promote plaque progression. However, for that approach there was no statistical significance both for WSS and PSS.

Chapter 5: Limitations

There are some limitations in this study that need to be considered. The first limitation is related to the co-registration of IVUS and OCT image data. That process is quite prone to errors since IVUS and OCT do not have the same sample frequency. Furthermore, it was observed that there were some cases where the lumen of the OCT and IVUS did not have the same shape. Although, these cases were excluded, still it is a limitation that needs to be considered for future studies.

The second limitation concerns the algorithm of the reconstruction of the 2D geometries. Kok et. al. designed the specific algorithm based on necrotic cores that had angle extension ranging from 35 – 75^{o} angle width [47]. In this study not all necrotic cores had an angle width smaller than a 75^{o} angle. It was observed that for necrotic cores with angle width larger than 90^{o} (> 90 ^{o}) the backside of the necrotic core was intersecting the front side of it and, thus, they excluded from the study.

A third limitation is that for the reconstruction of the 2D geometry calcifications were not included. Since the material properties of the calcifications are different than those used in this study, they may affect the stress calculations, as calcifications are more rigid and they can affect the load bearing; thus, cross-sections with calcifications were excluded.

The fourth limitation is that no patient-specific pressures were used for the stress calculations. This means that the contribution of the variable of pressure, which can be different from patient to patient, is not included. The data used in this project are valid, but they do not include the variety of the pressure; thus, the current model is simpler than the model that include patient-specific blood pressure.

Fifth, the effect of media and adventitia is completely ignored in this study. The thickness of media is so small and, thus, it was not included in the stress calculations. The contribution of adventitia can be ignored for the low values of pressure; however, as the pressure is increasing, the adventitia affect more the load bearing of the vessel [54], [55].

Sixth, aim of this study is to investigate the association between the biomechanical stresses, WSS and PSS, and the plaque progression; thus, there is no confirmation about

cause – effect relationship between those. The last limitation is that there is the need for studies with larger sample size in order to validate those results.

Chapter 6: Future perspectives

For the acquisition of the image data two catheters were used, one for OCT and one for IVUS. The co-registration was performed manually. However, it is believed by the writer that the utilization of one catheter that can perform both IVUS and OCT imaging simultaneously should be utilized. In the literature there are already a few studies about the combination of OCT and IVUS in one catheter [56]–[58]. This may reduce the procedure costs, since only one catheter will be needed to introduce into the patients. Moreover, it can make the process of co-registration easier, since it was reported that a catheter that combine OCT and IVUS can provide co-registered OCT and IVUS images in one pullback [58]. This may also provide insight on cases where the lumen of OCT and IVUS did not have the same shape. Nevertheless, based on the knowledge of the writer this type of catheter is no commercially available yet. Another thing that can be considered, if IVUS and OCT cannot be performed simultaneously with one catheter, is the automated co-registration. Currently in this project the co-registration was performed manually. However, in the literature there is a study that introduces an automated methodology for co-registration [16]. If this methodology is implemented then the whole process can be automated and the only requirement is the introduction of the image data from OCT and IVUS.

On top of that there is the necessity for a new version of the current algorithm of the necrotic core reconstruction, since there is the need for reconstruction of necrotic cores that have angle width larger than 90^o (> 90 ^{o}). A simple way to improve the current algorithm is to use more points. In the current version three points are being created based on the thickness of the necrotic core at the midcap (50%) and at the two sidecaps (25% and 75%). Instead of that approach it is believed that by the introduction of more points it will be feasible to reconstruct necrotic cores with angle width larger than 90^o (> 90^o). Secondly, the reconstruction algorithm should be able to reconstruct calcifications. Calcifications are characterized by higher stiffness compared to necrotic cores and increase the arterial stiffness [59]. If the calcifications are present in the intima, they will affect the intima stiffness. In a study of Akyildiz et. al. they observed that changes in the stiffness of intima in human coronary arteries can change the PSS [60].

Moreover, the contribution of media and adventitia in the stress calculation should be studied. Regarding the presence of calcifications in the media, they can affect differently the biomechanical stresses compared to the presence of calcifications in the intima [61]. The adventitia needs also to be included, since at high pressures the adventitia contributes to load bearing of the artery [54], [55].

The blood pressure is another variable that can increase the complexity of the model. While the current model is simpler since there is no patient-specific pressure, it will be very interesting to perform the same stress calculations but with patient-specific pressures. Afterwards, a comparison between those two models can be performed in order to check if the variety of the patient-specific blood pressure is contributing to the stress calculations and if it does, to what extent it is contributing.

Another parameter that can be considered is the time required for the stress calculations. On the current version of the pipeline the stress calculations of each cross-

section required roughly 10 minutes. In order to finish the stress calculations for all the cross-sections (1042) it took about 7 days. However, if we consider the new version of algorithm, which will introduce more components on the 2D geometries, and we include the media and adventitia, the time for the stress calculations needed for each cross-section will be increased dramatically. On top of that, assuming the same sample size, if we include all the cross-sections that were removed due to different limitations in the stress calculations, the number of available cross-sections doubles (2481). Thus, time starts to become a parameter we may need to consider. In order to tackle this issue the whole process of reconstruction and stress calculation can be performed utilizing parallel programming. Both Matlab and ABAQUS support parallel processing; thus, it is suggested to utilize the feature in order to reduce the total process time.

Lastly, the implementation of neural networks may contribute in the prediction of plaque progression. A neural network can be trained in order to predict the plaque development using as inputs a variety of parameters. Such parameters are the biomechanical stresses, the wall thickness of the patient's vessel and other characteristics of the patient such as diet and physical activity. The successful implementation of a neural network can be practically useful, since the doctors will be able to introduce the patient's data to it and the neural network will predict the plaque progression of the patient. Based on that prediction the doctors would be able to decide about the medications of the patient.

Chapter 7: Conclusions

During this project a new methodology was introduced that utilizes image data of human coronary arteries from OCT and IVUS in order to perform stress calculations. It is a new approach for performing stress calculations and the study of plaque development in living patients. On top of that it is the first time that the necrotic cores from coronary arteries of living patients are reconstructed. This methodology allows the reconstruction of more components of the human coronary arteries, which may lead to a better understanding about the development and progression of the atherosclerosis in the human coronary arteries.

Furthermore, it was shown that different image modalities can be combined in order to provide more information and higher accuracy than by utilizing only one image modality. Each current image modality is characterized by a set of advantages and disadvantages. If complementary image modalities are used together, like OCT and IVUS, those disadvantages can be overcome resulting in more accurate stress calculations.

Regarding the results it was demonstrated that high PSS might promote plaque progression, but in this study there was no statistically significant effect. Low WSS promoted plaque development as there was a statistically significant effect. For the combination of those stress it was observed that low WSS combined with any level of PSS had the most effect on plaque progression using the vessel specific approach. However, since the effect of plaque structural stress is not statistically significant, it can be said the effect of the combination of those biomechanical stresses can all be explained by wall shear stress. For the absolute thresholds approach neither PSS nor WSS were statistically significant. Lastly, the results should be implemented with caution, since more data are required to draw firm conclusions on the relationship between biomechanical stress and plaque progression in human coronary arteries.

Appendix A

The decision of whom is eligible to participate is based on the following inclusion/exclusion.

Inclusion criteria:

- Age > 18 years.
- Ability to provide informed consent.
- At least one non-stented non-culprit coronary vessel'

Exclusion criteria:

- Three-vessel disease
- Previous coronary artery bypass graft surgery
- Left ventricular ejection fraction < 30%
- Atrial fibrillation
- Renal insufficiency (creatinine clearing < 50 ml/min)

Patient characteristics	
Number of patients	48
Age, years	61 ± 8.9
Men, n(%)	42 (87.5%)
Body mass index	27 ± 4.6
Diabetes mellitus, n (%)	8 (16.7%)
Hypertension, n(%)	14 (29.2%)
Dyslipidemia, n(%)	23 (47.9%)
Current smoking, n(%)	12 (25%)
Positive family history, n(%)	17 (35.4%)
Previous MI, n(%)	9 (18.8%)
Previous PCI, n(%)	11 (22.9%)
LDL (mmol/L)	2.8 [2.1 – 3.3]

Table 9: Table with patient characteristics. MI stands for myocardial infarction. PCI stands for percutaneous coronary intervention.

Vessel characteristics	
Imaged studied vessels	49
Length (mm)	53.15 ± 18.36
LAD, n(%)	19 (38.8 %)
LCX, n(%)	13 (26,5%)
RCA, n(%)	17 (34,7%)

Table 10: Table with vessel characteristics. LAD is the left anterior descending coronary artery, LCX is the left circumflex coronary artery and RCA is the right coronary artery.

Appendix B

During imaging of the arteries, the plaques that are present in them are pressurized by the in-vivo blood pressure; thus, in the arteries there is a certain initial pressure which is greater than 0 (unpressurized state). If stress calculations based only on the geometry of the vessel are performed, this initial pressure is neglected. The Backward Incremental method does not neglect the initial pressure and, thus, can provide more accurate results [50]. During that method the systolic pressure is achieved in 18 steps. For the steps 1 until 15 the intraluminal pressure was increased and at the step 16 the diastolic pressure is achieved. In each step, stress analysis is performed. The calculated stress resulted from the stress analysis are used as initial stress boundary condition for the next steps and they applied on the respective nodes. During the steps 1 till 15 the geometry that is used is the one that was measured during imaging and deformations of the geometry are ignored. At the step 16 the diastolic pressure is applied. The systolic pressure is achieved at step 18. During steps 16 till 18 the deformation of the geometry is not ignored. This whole process can be described in the following part:

$\Omega_o = \Omega_{measured}$

$\mathbf{F}_{0,0} = \mathbf{I}$

$\boldsymbol{\sigma}_0 = 0$

for $n = 1{:}\,18$

$\left(\mathbf{F}_{n-1,n}, \boldsymbol{\delta\sigma}_n\right) = f\left(\Omega_{n-1}, \mathbf{F}_{0,n-1}, \boldsymbol{\sigma}_{n-1}, p_n, G\right)$

if $(n < 16)$ then $\Omega_n = \Omega_{n-1}$

if $(n \geq 16)$ then $\Omega_n = \Omega_n\left(\mathbf{F}_{n-1,n}, \Omega_{n-1}\right)$

$\mathbf{F}_{0,n} = \mathbf{F}_{0,n-1}\mathbf{F}_{n-1,n}$

$\boldsymbol{\sigma}_n = \boldsymbol{\sigma}_{n-1} + \boldsymbol{\delta\sigma}_n$

end

where Ω_n is the geometry at the step n, $\mathbf{F}_{a,b}$ is the deformation tensor between steps a and b, $\mathbf{I}$ is the unity tensor, $\boldsymbol{\sigma}_n$ is stress tensor at step n, p_n is the applied pressure at the step n and G describes the material parameters.

Appendix C

PSS	Mean	Standard error
Low	0.028	0.005
Medium	0.037	0.004
High	0.049	0.005

Table 11: The values of the case of division of PSS based on the percentiles of values of each vessel. Those values are from the Figure 14.

WSS	Mean	Standard error
Low	0.054	0.004
Medium	0.020	0.005
High	0.016	0.005

Table 12: The values of the case of division of WSS based on the percentiles of values of each vessel. Those values are from the Figure 15.

PSS	WSS	Mean	Standard error
Low	**Low**	0.051	0.008
	Medium	0.021	0.009
	High	-0.003	0.011
Medium	**Low**	0.062	0.007
	Medium	0.024	0.009
	High	0.022	0.011
High	**Low**	0.061	0.008
	Medium	0.033	0.010
	High	0.034	0.009

Table 13: The mean values and the standard deviations for all combinations of WSS and PSS of the Figure 16. The division is based on the percentiles of values of each vessel.

PSS	Mean	Standard error
Low	0.024	0.006
Medium	0.032	0.005
High	0.054	0.008

Table 14: The values of the case of division of PSS based on the percentiles of values of whole range. Those values are from the Figure 17.

WSS	Mean	Standard error
Low	0.052	0.006
Medium	0.024	0.006
High	0.026	0.009

Table 15: The values of the case of division of WSS based on the percentiles of values of whole range. Those values are from the Figure 18.

PSS	WSS	Mean	Standard error
Low	**Low**	0.055	0.010
	Medium	0.024	0.009
	High	0.016	0.014
Medium	**Low**	0.038	0.010
	Medium	0.029	0.011
	High	0.038	0.012
High	**Low**	0.053	0.011
	Medium	0.046	0.011
	High	0.081	0.013

Table 16: The mean values and the standard deviations for all combinations of WSS and PSS of the Figure 19. The division is based on the percentiles of values of whole range.

References

[1] “Cardiovascular diseases (CVDs).” [Online]. Available: https://www.who.int/news-room/fact-sheets/detail/cardiovascular-diseases-(cvds).

[2] S. Mundi *et al.*, “Endothelial permeability, LDL deposition, and cardiovascular risk factors-a review,” *Cardiovasc. Res.*, vol. 114, no. 1, pp. 35–52, 01 2018, doi: 10.1093/cvr/cvx226.

[3] G. K. Hansson and A. Hermansson, “The immune system in atherosclerosis,” *Nat. Immunol.*, vol. 12, no. 3, pp. 204–212, Mar. 2011, doi: 10.1038/ni.2001.

[4] A. C. Newby, “Matrix metalloproteinases regulate migration, proliferation, and death of vascular smooth muscle cells by degrading matrix and non-matrix substrates,” *Cardiovasc. Res.*, vol. 69, no. 3, pp. 614–624, Feb. 2006, doi: 10.1016/j.cardiores.2005.08.002.

[5] M. A. Gimbrone and G. García-Cardeña, “Endothelial Cell Dysfunction and the Pathobiology of Atherosclerosis,” *Circ. Res.*, vol. 118, no. 4, pp. 620–636, Feb. 2016, doi: 10.1161/CIRCRESAHA.115.306301.

[6] P. R. Moreno, “Vulnerable Plaque: Definition, Diagnosis, and Treatment,” *Cardiol. Clin.*, vol. 28, no. 1, pp. 1–30, Feb. 2010, doi: 10.1016/j.ccl.2009.09.008.

[7] F. Otsuka, K. Sakakura, K. Yahagi, M. Joner, and R. Virmani, “Has our understanding of calcification in human coronary atherosclerosis progressed?,” *Arterioscler. Thromb. Vasc. Biol.*, vol. 34, no. 4, pp. 724–736, Apr. 2014, doi: 10.1161/ATVBAHA.113.302642.

[8] A. Shioi and Y. Ikari, “Plaque Calcification During Atherosclerosis Progression and Regression,” *J. Atheroscler. Thromb.*, vol. 25, no. 4, pp. 294–303, Apr. 2018, doi: 10.5551/jat.RV17020.

[9] Lutgens Esther *et al.*, “Atherosclerotic Plaque Rupture,” *Arterioscler. Thromb. Vasc. Biol.*, vol. 23, no. 12, pp. 2123–2130, Dec. 2003, doi: 10.1161/01.ATV.0000097783.01596.E2.

[10] C. Fortini, C. Caliceti, G. Aquila, M. Morelli, R. Pavasini, and P. Rizzo, “The Role of the Notch Pathway in Atherosclerosis,” Sep. 2015. doi: 10.13140/RG.2.1.1456.0489.

[11] I. Cuadrado *et al.*, “Preclinical models of atherosclerosis. The future of Hybrid PET/MR technology for the early detection of vulnerable plaque.,” *Expert Rev. Mol. Med.*, 2016, doi: 10.1017/erm.2016.5.

[12] G. van Soest, L. Marcu, B. E. Bouma, and E. Regar, “Intravascular imaging for characterization of coronary atherosclerosis,” *Curr. Opin. Biomed. Eng.*, vol. 3, pp. 1–12, Sep. 2017, doi: 10.1016/j.cobme.2017.07.001.

[13] G. S. Mintz, “Intravascular imaging of coronary calcification and its clinical implications,” *JACC Cardiovasc. Imaging*, vol. 8, no. 4, pp. 461–471, Apr. 2015, doi: 10.1016/j.jcmg.2015.02.003.

[14] X. Guo *et al.*, “Combining IVUS and Optical Coherence Tomography for More Accurate Coronary Cap Thickness Quantification and Stress/Strain Calculations: A Patient-Specific Three-Dimensional Fluid-Structure Interaction Modeling Approach,” *J. Biomech. Eng.*, vol. 140, no. 4, 01 2018, doi: 10.1115/1.4038263.

[15] A. Nair, B. D. Kuban, E. M. Tuzcu, P. Schoenhagen, S. E. Nissen, and D. G. Vince, “Coronary plaque classification with intravascular ultrasound

radiofrequency data analysis," *Circulation*, vol. 106, no. 17, pp. 2200–2206, Oct. 2002, doi: 10.1161/01.cir.0000035654.18341.5e.

[16] D. S. Molony, L. H. Timmins, E. Rasoul-Arzrumly, H. Samady, and D. P. Giddens, "Evaluation of a framework for the co-registration of intravascular ultrasound and optical coherence tomography coronary artery pullbacks," *J. Biomech.*, vol. 49, no. 16, pp. 4048–4056, Dec. 2016, doi: 10.1016/j.jbiomech.2016.10.040.

[17] P. K. Cheruvu *et al.*, "Frequency and distribution of thin-cap fibroatheroma and ruptured plaques in human coronary arteries: a pathologic study," *J. Am. Coll. Cardiol.*, vol. 50, no. 10, pp. 940–949, Sep. 2007, doi: 10.1016/j.jacc.2007.04.086.

[18] A. J. Brown, Z. Teng, P. C. Evans, J. H. Gillard, H. Samady, and M. R. Bennett, "Role of biomechanical forces in the natural history of coronary atherosclerosis," *Nat. Rev. Cardiol.*, vol. 13, no. 4, pp. 210–220, Apr. 2016, doi: 10.1038/nrcardio.2015.203.

[19] D. Shav, R. Gotlieb, U. Zaretsky, D. Elad, and S. Einav, "Wall shear stress effects on endothelial-endothelial and endothelial-smooth muscle cell interactions in tissue engineered models of the vascular wall," *PloS One*, vol. 9, no. 2, p. e88304, 2014, doi: 10.1371/journal.pone.0088304.

[20] S. Xu, X. Li, K. B. LaPenna, S. D. Yokota, S. Huke, and P. He, "New insights into shear stress-induced endothelial signalling and barrier function: cell-free fluid versus blood flow," *Cardiovasc. Res.*, vol. 113, no. 5, pp. 508–518, Apr. 2017, doi: 10.1093/cvr/cvx021.

[21] J. Zhou *et al.*, "Regulation of vascular smooth muscle cell turnover by endothelial cell-secreted microRNA-126: role of shear stress," *Circ. Res.*, vol. 113, no. 1, pp. 40–51, Jun. 2013, doi: 10.1161/CIRCRESAHA.113.280883.

[22] H. Samady *et al.*, "Coronary artery wall shear stress is associated with progression and transformation of atherosclerotic plaque and arterial remodeling in patients with coronary artery disease," *Circulation*, vol. 124, no. 7, pp. 779–788, Aug. 2011, doi: 10.1161/CIRCULATIONAHA.111.021824.

[23] C. Costopoulos *et al.*, "Impact of combined plaque structural stress and wall shear stress on coronary plaque progression, regression, and changes in composition," *Eur. Heart J.*, vol. 40, no. 18, pp. 1411–1422, May 2019, doi: 10.1093/eurheartj/ehz132.

[24] X. Liu *et al.*, "Prediction of coronary plaque progression using biomechanical factors and vascular characteristics based on computed tomography angiography," *Comput. Assist. Surg.*, vol. 22, no. sup1, pp. 286–294, Oct. 2017, doi: 10.1080/24699322.2017.1389407.

[25] G. A. Rodriguez-Granillo *et al.*, "Plaque Composition and its Relationship With Acknowledged Shear Stress Patterns in Coronary Arteries," *J. Am. Coll. Cardiol.*, vol. 47, no. 4, pp. 884–885, Feb. 2006, doi: 10.1016/j.jacc.2005.11.027.

[26] Eshtehardi Parham *et al.*, "Association of Coronary Wall Shear Stress With Atherosclerotic Plaque Burden, Composition, and Distribution in Patients With Coronary Artery Disease," *J. Am. Heart Assoc.*, vol. 1, no. 4, p. e002543, doi: 10.1161/JAHA.112.002543.

[27] J. Wentzel *et al.*, "In vivo assessment of the relationship between shear stress and necrotic core in early and advanced coronary artery disease,"

EuroIntervention: journal of EuroPCR in collaboration with the Working Group on Interventional Cardiology of the European Society of Cardiology, vol. 9, no. 8, pp. 989-995, Mar. 2013.

[28] Vergallo Rocco *et al.*, "Endothelial Shear Stress and Coronary Plaque Characteristics in Humans," *Circ. Cardiovasc. Imaging*, vol. 7, no. 6, pp. 905–911, Nov. 2014, doi: 10.1161/CIRCIMAGING.114.001932.

[29] C. Costopoulos *et al.*, "Plaque Rupture in Coronary Atherosclerosis Is Associated With Increased Plaque Structural Stress," *JACC Cardiovasc. Imaging*, vol. 10, no. 12, pp. 1472–1483, Dec. 2017, doi: 10.1016/j.jcmg.2017.04.017.

[30] D. Tang *et al.*, "A negative correlation between human carotid atherosclerotic plaque progression and plaque wall stress: in vivo MRI-based 2D/3D FSI models," *J. Biomech.*, vol. 41, no. 4, pp. 727–736, 2008, doi: 10.1016/j.jbiomech.2007.11.026.

[31] Tang Dalin *et al.*, "Sites of Rupture in Human Atherosclerotic Carotid Plaques Are Associated With High Structural Stresses," *Stroke*, vol. 40, no. 10, pp. 3258–3263, Oct. 2009, doi: 10.1161/STROKEAHA.109.558676.

[32] A. J. Brown *et al.*, "Plaque Structural Stress Estimations Improve Prediction of Future Major Adverse Cardiovascular Events After Intracoronary Imaging," *Circ. Cardiovasc. Imaging*, vol. 9, no. 6, 2016, doi: 10.1161/CIRCIMAGING.115.004172.

[33] Teng Zhongzhao *et al.*, "Coronary Plaque Structural Stress Is Associated With Plaque Composition and Subtype and Higher in Acute Coronary Syndrome," *Circ. Cardiovasc. Imaging*, vol. 7, no. 3, pp. 461–470, May 2014, doi: 10.1161/CIRCIMAGING.113.001526.

[34] C. Costopoulos *et al.*, "Intravascular ultrasound and optical coherence tomography imaging of coronary atherosclerosis," *Int. J. Cardiovasc. Imaging*, vol. 32, no. 1, pp. 189–200, Jan. 2016, doi: 10.1007/s10554-015-0701-3.

[35] S.-J. Kang *et al.*, "Plaque structural stress assessed by virtual histology-intravascular ultrasound predicts dynamic changes in phenotype and composition of untreated coronary artery lesions," *Atherosclerosis*, vol. 254, pp. 85–92, Nov. 2016, doi: 10.1016/j.atherosclerosis.2016.09.072.

[36] M. B. Dancu, D. E. Berardi, J. P. Vanden Heuvel, and J. M. Tarbell, "Atherogenic Endothelial Cell eNOS and ET-1 Responses to Asynchronous Hemodynamics are Mitigated by Conjugated Linoleic Acid," *Ann. Biomed. Eng.*, vol. 35, no. 7, pp. 1111–1119, Jul. 2007, doi: 10.1007/s10439-007-9290-1.

[37] H. M. Loree, R. D. Kamm, R. G. Stringfellow, and R. T. Lee, "Effects of fibrous cap thickness on peak circumferential stress in model atherosclerotic vessels," *Circ. Res.*, vol. 71, no. 4, pp. 850–858, Oct. 1992, doi: 10.1161/01.res.71.4.850.

[38] H. Gao and Q. Long, "Effects of varied lipid core volume and fibrous cap thickness on stress distribution in carotid arterial plaques," *J. Biomech.*, vol. 41, no. 14, pp. 3053–3059, Oct. 2008, doi: 10.1016/j.jbiomech.2008.07.011.

[39] J. F. Bentzon and E. Falk, "Chapter 47 - Atherosclerosis, Vulnerable Plaques, and Acute Coronary Syndromes," in *Genomic and Personalized Medicine (Second Edition)*, G. S. Ginsburg and H. F. Willard, Eds. Academic Press, 2013, pp. 530–539.

[40] Virmani Renu, Kolodgie Frank D., Burke Allen P., Farb Andrew, and Schwartz Stephen M., “Lessons From Sudden Coronary Death,” *Arterioscler. Thromb. Vasc. Biol.*, vol. 20, no. 5, pp. 1262–1275, May 2000, doi: 10.1161/01.ATV.20.5.1262.

[41] R. Virmani, E. R. Ladich, A. P. Burke, and F. D. Kolodgie, “Histopathology of carotid atherosclerotic disease,” *Neurosurgery*, vol. 59, no. 5 Suppl 3, pp. S219-227; discussion S3-13, Nov. 2006, doi: 10.1227/01.NEU.0000239895.00373.E4.

[42] S. E. Nissen, “IVUS Virtual Histology: Unvalidated Gimmick or Useful Technique?∗,” *J. Am. Coll. Cardiol.*, vol. 67, no. 15, pp. 1784–1785, Apr. 2016, doi: 10.1016/j.jacc.2016.02.037.

[43] “Intravascular Ultrasound (IVUS).” http://www.ptca.org/ivus/ivus.html (accessed Feb. 07, 2020).

[44] O. Bayturan *et al.*, “Attenuated Plaque at Nonculprit Lesions in Patients Enrolled in Intravascular Ultrasound Atherosclerosis Progression Trials,” *JACC Cardiovasc. Interv.*, vol. 2, no. 7, pp. 672–678, Jul. 2009, doi: 10.1016/j.jcin.2009.05.007.

[45] G. J. Tearney *et al.*, “Consensus Standards for Acquisition, Measurement, and Reporting of Intravascular Optical Coherence Tomography Studies: A Report From the International Working Group for Intravascular Optical Coherence Tomography Standardization and Validation,” *J. Am. Coll. Cardiol.*, vol. 59, no. 12, pp. 1058–1072, Mar. 2012, doi: 10.1016/j.jacc.2011.09.079.

[46] H. Ikenaga *et al.*, “Longitudinal extent of lipid pool assessed by optical coherence tomography predicts microvascular no-reflow after primary percutaneous coronary intervention for ST-segment elevation myocardial infarction,” *J. Cardiol.*, vol. 62, no. 2, pp. 71–76, Aug. 2013, doi: 10.1016/j.jjcc.2013.03.005.

[47 A. M. Kok, L. Speelman, R. Virmani, A. F. W. van der Steen, F. J. H. Gijsen, and J. J. Wentzel, “Peak cap stress calculations in coronary atherosclerotic plaques with an incomplete necrotic core geometry,” *Biomed. Eng. Online*, vol. 15, no. 1, p. 48, May 2016, doi: 10.1186/s12938-016-0162-5.

[48] P. Badel, S. Avril, M. A. Sutton, and S. M. Lessner, “Numerical simulation of arterial dissection during balloon angioplasty of atherosclerotic coronary arteries,” *J. Biomech.*, vol. 47, no. 4, pp. 878–889, Mar. 2014, doi: 10.1016/j.jbiomech.2014.01.009.

[49] A. Kelly-Arnold, N. Maldonado, D. Laudier, E. Aikawa, L. Cardoso, and S. Weinbaum, “Revised microcalcification hypothesis for fibrous cap rupture in human coronary arteries,” *Proc. Natl. Acad. Sci.*, vol. 110, no. 26, pp. 10741–10746, Jun. 2013, doi: 10.1073/pnas.1308814110.

[50] L. Speelman *et al.*, “Initial stress in biomechanical models of atherosclerotic plaques,” *J. Biomech.*, vol. 44, no. 13, pp. 2376–2382, Sep. 2011, doi: 10.1016/j.jbiomech.2011.07.004.

[51] G. A. Holzapfel, G. Sommer, C. T. Gasser, and P. Regitnig, “Determination of layer-specific mechanical properties of human coronary arteries with nonatherosclerotic intimal thickening and related constitutive modeling,” *Am. J. Physiol. Heart Circ. Physiol.*, vol. 289, no. 5, pp. H2048-2058, Nov. 2005, doi: 10.1152/ajpheart.00934.2004.

[52] H. M. Loree, B. J. Tobias, L. J. Gibson, R. D. Kamm, D. M. Small, and R. T. Lee, “Mechanical properties of model atherosclerotic lesion lipid pools,” *Arterioscler. Thromb. J. Vasc. Biol.*, vol. 14, no. 2, pp. 230–234, Feb. 1994, doi: 10.1161/01.atv.14.2.230.

[53] A. P. C. Choi and Y. P. Zheng, “Estimation of Young’s modulus and Poisson’s ratio of soft tissue from indentation using two different-sized indentors: finite element analysis of the finite deformation effect,” *Med. Biol. Eng. Comput.*, vol. 43, no. 2, pp. 258–264, Mar. 2005, doi: 10.1007/bf02345964.

[54] C. A. J. Schulze-Bauer, P. Regitnig, and G. A. Holzapfel, “Mechanics of the human femoral adventitia including the high-pressure response,” *Am. J. Physiol.-Heart Circ. Physiol.*, vol. 282, no. 6, pp. H2427–H2440, Jun. 2002, doi: 10.1152/ajpheart.00397.2001.

[55] G. Sommer, P. Regitnig, L. Költringer, and G. A. Holzapfel, “Biaxial mechanical properties of intact and layer-dissected human carotid arteries at physiological and supraphysiological loadings,” *Am. J. Physiol.-Heart Circ. Physiol.*, vol. 298, no. 3, pp. H898–H912, Dec. 2009, doi: 10.1152/ajpheart.00378.2009.

[56] X. Li *et al.*, “Integrated IVUS-OCT Imaging for Atherosclerotic Plaque Characterization,” *IEEE J. Sel. Top. Quantum Electron. Publ. IEEE Lasers Electro-Opt. Soc.*, vol. 20, no. 2, p. 7100108, 2014, doi: 10.1109/JSTQE.2013.2274724.

[57] J. Li *et al.*, “Ultrafast optical-ultrasonic system and miniaturized catheter for imaging and characterizing atherosclerotic plaques in vivo,” *Sci. Rep.*, vol. 5, no. 1, pp. 1–7, Dec. 2015, doi: 10.1038/srep18406.

[58] J. Toma *et al.*, “TCT-569 Validation of Novel Combined IVUS/OCT Catheter using Ex-Vivo Samples: Qualitative Examination of Human Cadaver Specimens,” *J. Am. Coll. Cardiol.*, vol. 68, no. 18 Supplement, p. B230, Feb. 2019, doi: 10.1016/j.jacc.2016.09.707.

[59] J. Nemcsik, I. Kiss, and A. Tislér, “Arterial stiffness, vascular calcification and bone metabolism in chronic kidney disease,” *World J. Nephrol.*, vol. 1, no. 1, pp. 25–34, Feb. 2012, doi: 10.5527/wjn.v1.i1.25.

[60] A. C. Akyildiz *et al.*, “Effects of intima stiffness and plaque morphology on peak cap stress,” *Biomed. Eng. Online*, vol. 10, p. 25, Apr. 2011, doi: 10.1186/1475-925X-10-25.

[61] G. M. London, A. P. Guérin, S. J. Marchais, F. Métivier, B. Pannier, and H. Adda, “Arterial media calcification in end-stage renal disease: impact on all-cause and cardiovascular mortality,” *Nephrol. Dial. Transplant. Off. Publ. Eur. Dial. Transpl. Assoc. - Eur. Ren. Assoc.*, vol. 18, no. 9, pp. 1731–1740, Sep. 2003, doi: 10.1093/ndt/gfg414.